Models of the mantle shear velocity and discontinuities in the pattern of lateral heterogeneities

Yu J. Gu, Adam M. Dziewonski, Weijia Su, and Göran Ekström

Department of Earth and Planetary Sciences, Harvard University, Cambridge, Massachusetts

Abstract. Resolution of the pattern of large-scale shear velocity variations above and below the known and postulated mantle discontinuities could provide constraints on the nature of mineral phase transitions, changes in composition, and the scale of mantle convection. To achieve good resolution across a full range of depths, we use a diversified data set consisting of body and mantle wave waveforms, travel times, and surface wave phase velocities. Our main focus is on the 670-km discontinuity, long presumed to be an important barrier, or impediment, to whole mantle convection. Our data set has a relatively high radial resolution throughout the mantle; in the transition zone and some 200 km below it, the long period waveforms, dominated by multiple surface reflections, make a particularly important contribution. We use a local spline support to parameterize the model; this allows us to obtain a smooth model (twice differentiable) and simplifies calculation of the model and its derivatives in applications such as three-dimensional ray tracing. In one inversion we use a continuous radial representation throughout the mantle; in the other, a discontinuity is allowed across the 670-km boundary. Both models suggest that the long-wavelength anomalies of the transition zone and the mantle below 750 km are significantly different. Near 670 km these two models display notable differences in the peak amplitudes and lateral scales of major anomalies. The degree 2 spherical harmonic, which dominates the large-scale shear velocities in the transition zone, is strongly attenuated at the top of the lower mantle where the power spectrum is essentially white. Resolution tests show that these results are robust, which suggests a possible reorganization of the flow between the upper and lower mantle. At other depths the power spectra of our models as a function of depth indicate a modest change near 400 km, where the dominating effect of degree 5 (shields) is replaced by degree 2 (slabs). The power of the heterogeneity in at mid-mantle depths is low and nearly flat as a function of spherical harmonic degree up to $\ell = 12$, with no detectable change near 1000 km. The increase of the power in the lowermost mantle is rather gradual, not characteristic of a discontinuous change. Cross sections of our models at major subduction zones indicate that major downwelling of cold slab material may occur at some locations. On the other hand, there are numerous examples of an abrupt change of the sign of the velocity anomalies across the 670-km discontinuity.

1. Introduction

Radial and lateral variations of mantle shear velocities near the seismic discontinuity between upper and lower mantle contain important information about the chemical and dynamical properties in the Earth's mantle. For example, *Tackley et al.* [1993, 1994] develop a model of convection characterized by accumulating subducted material in the transition zone and then breaking the barrier in a sudden avalanche. This model implies a discontinuity in the pattern of lateral heterogene-

ity. On the other hand, a model by *Bunge et al.* [1996] introduces a 30-fold contrast in viscosity at the 670-km discontinuity and obtains a similar effect by shifting the peak of the power spectrum toward low wavelengths, but the thermal heterogeneity in the model is continuous. We use the value of 670 km for the depth of the boundary between the upper and lower mantle because the Preliminary Reference Earth Model (PREM) [*Dziewonski and Anderson*, 1981] is used as a reference model, although we recognize that its average depth is closer to 660 km [*Revenaugh and Jordan*, 1991].

For almost two decades, various types of travel time and long period surface and body wave waveform measurements have been analyzed to develop more accurate models of the three-dimensional (3-D) shear velocity

variations [e.g., *Masters et al.*, 1982, 1992, 1996; *Woodhouse and Dziewonski*, 1984, 1986, 1989; *Tanimoto*, 1990; *Woodward and Masters*, 1991a, 1991b; *Zhang and Tanimoto*, 1993; *Dziewonski et al.*, 1993; *Su et al.*, 1994; *Li and Romanowicz*, 1996; *Su and Dziewonski*, 1997; *Liu and Dziewonski*, 1998; *Ekström and Dziewonski*, 1998]. These tomographic studies laid the groundwork for characterizing the complex nature of the transition zone heterogeneities and their relation to mantle flow. Identification and analysis of secondary reflected and converted phases furthered our understanding of this region [e.g., *Revenaugh and Jordan*, 1989, 1991; *Shearer and Masters*, 1992; *Shearer*, 1993; *Gossler and Kind*, 1996; *Flanagan and Shearer*, 1998; *Gu et al.*, 1998]. One important observation from these studies is the long-wavelength depression of the global topography of the 670-km discontinuity in the vicinity of major subduction zones [*Revenaugh and Jordan*, 1989; *Shearer and Masters*, 1992]. The spatial location of the depression is well correlated with the large-scale fast shear velocity anomalies within the transition zone [*Masters et al.*, 1982; *van der Hilst et al.*, 1991; *Su et al.*, 1994], and hence has been associated with the accumulation of cold slab material at the endothermic phase boundary [*Shearer*, 1993; *Phipps Morgan and Shearer*, 1993].

A change in the long-wavelength pattern of shear velocities in the degree 8 continuous (S8/WM13) and split (S8/U4L8) models near 670 km was reported by *Woodward et al.* [1993] and discussed in the context of mantle flow by *Woodward et al.* [1994]. However, because of differences in the data sensitivity and modeling methods, controversies persist with regard to the location, amplitude, and spatial extent of the large-scale shear velocity structure near 670 km. Furthermore, although the 670-km discontinuity has been widely associated with the phase transition from γ-spinel to perovskite + magnesiowüstite, how this transition affects the convective transport of mass and heat between the upper and lower mantle is still a matter of debate. Recent findings from joint inversions of seismic and geoid observations using global basis functions [*Forte and Woodward*, 1997] reveal the existence of a family of 3-D models that predict layered convection.

This study provides an image of mantle shear velocity variations using a novel parameterization and a significantly expanded set of seismic data. The emphasis is on the structure near the boundary between the upper and lower mantle, where models with one set of B spline radial basis functions for the whole mantle (continuous model) are compared with those of two distinct sets of B spline functions (split model) across the 670-km boundary. In this study we demonstrate the existence of a model with a significant change in the pattern of heterogeneity across the 670-km discontinuity. This does not mean that such a model is unique. It is possible to find a model with a continuous change across this discontinuity that satisfies the observations equally well.

However, a wide range of evidence that the subducted slab is subjected to deformation in the transition zone provides a motivation for testing the hypothesis that it is possible to obtain a model that satisfies observations and is consistent with a major perturbation in the flow pattern.

A second issue is the potential existence of additional boundaries within the mantle that may affect the global flow pattern. One such boundary has been proposed for the 900–1100 km depth range [*Kawakatsu and Niu*, 1994; *van der Hilst and Kárason*, 1999] and another in the vicinity of 1800 km (*Su et al.* [1994] from *S*-wave data and *van der Hilst and Kárason* [1999] from *P* wave data). The suggestion of the latter has been used by *Kellogg et al.* [1999] in support of a hypothesis of a deep compositional discontinuity in the mantle. Our modeling using an expanded data set provides further constraints on these potential boundaries in the lower mantle.

2. Model Parameterization

The most frequent forms of representation of 3-D models use either local parameterization by blocks, within which the velocity perturbation is constant, or global parameterization by expansion in spherical harmonics to describe horizontal variations and Legendre or Chebyshev polynomials for the radial variations. A hybrid form of expansion was used by *Masters et al.* [1996] and *Liu and Dziewonski* [1998], who combined spherical harmonics with radial B splines. There is a significant variation in resolution with depth and it is difficult to account for it using global basis functions. The advantage of the local representation is mostly its efficiency: the data for a particular path can be represented by a linear combination of contributions from the relatively few blocks traversed by a ray. Hence a very large system of unknowns can be solved numerically using iterative techniques. One disadvantage of the "block" approach is that such models are rough and cannot be used to compute 3-D ray paths without introducing a smoothing algorithm.

A disadvantage of the global expansion is that it can be computationally expensive, particularly for high-order expansions, both in obtaining the model and in applying it when the point values have to be evaluated frequently. The orthogonal basis functions of this expansion, however, provide very stable solutions for the long-wavelength part of the model. Since all the seismic data used in 3-D inversions are a result of integration either along a ray path or over a volume, the average magnitude of a diagonal element of the inner product matrix is, roughly, proportional to $(\ell + 1)^{-2}$, where ℓ is the degree of a spherical harmonic. This means that the low-degree spherical harmonic coefficients are associated with the largest eigenvalues and can be determined accurately even if the sampling of the volume is

moderately uneven. This is quite important because the spectrum of lateral heterogeneity in the Earth is dominated by the low-degree harmonics [*Su and Dziewonski*, 1991]. In this paper we apply a local support representation which combines some of the advantages of both methods discussed above. The model is represented by

$$\frac{\delta v(r,\theta,\phi)}{v_0} = \sum_{i,j} C_{ij} S_j(\theta,\phi) B_i(r), \qquad (1)$$

where C_{ij} is the unknown coefficient, $S_j(\theta,\phi)$ is the jth spherical spline, and $B_i(r)$ is the ith radial spline.

In general, the differences in the modeling results using local and global parameterizations with comparable degrees of freedom are relatively small. Parameterization using local basis functions, however, enables convenient computation and storage of sparse **A** matrices for different data sets since only adjacent cells have nonzero contributions. An alternative approach was proposed by *Tarantola and Valette* [1982] and was later applied to the continuous case for regional [*Montagner*, 1986] and global studies [*Montagner and Tanimoto*, 1991] of 3-D mantle structure. This algorithm is not as efficient when the data set is large as the number of unknowns is equal to the number of data.

We consider only isotropic velocity variations in this study, though anisotropy has been shown to be important in the shallow mantle [*Montagner and Tanimoto*, 1990, 1991; *Ekström and Dziewonski*, 1998]. In particular, the effect of radial anisotropy can be strong in the upper 200 km. It is unlikely, however, that the presence of anisotropy can significantly bias our results due to its reduced level below 300 km.

2.1. Horizontal Parameterization

We parameterize the lateral shear velocity variations in terms of spherical B splines [*Wang and Dahlen*, 1995], centered at 362 nearly uniformly distributed knots (Figure 1a). The number of free parameters for such an expansion is nearly the same as that of a degree-18 spherical harmonic expansion (361). If the average distance between two neighboring knots is h, then these spline functions can be calculated from

$$S_j(\Delta) = \begin{cases} \frac{3}{4}(\frac{\Delta}{h})^3 - \frac{3}{2}(\frac{\Delta}{h})^2 + 1, & \Delta \leq h \\ -\frac{1}{4}(2 - \frac{\Delta}{h})^3, & h \leq \Delta \leq 2h \\ 0, & \Delta > 2h, \end{cases} \qquad (2)$$

where Δ is the arc distance of a point with coordinates (θ,ϕ) from the jth knot (θ_j,ϕ_j) [*de Boor*, 1978; *Lan-*
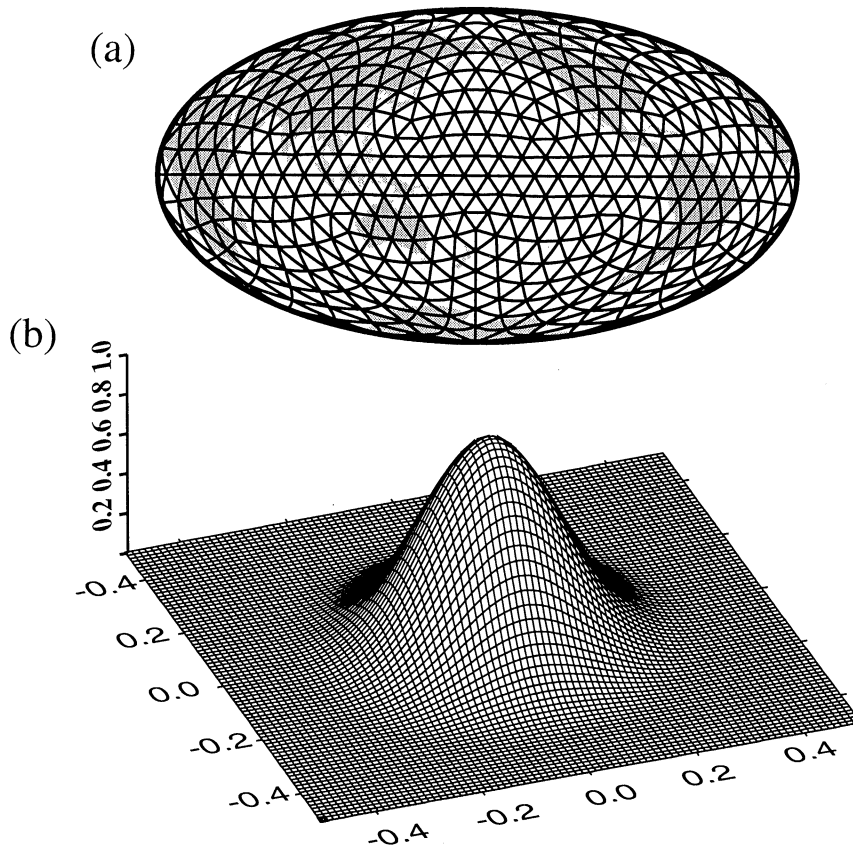
Figure 1. (a) Triangular tessellation. Earth is divided into 362 nearly equal-area triangles. Each knot location coincides with the center of a spherical B spline. This expansion is essentially equivalent to a spherical harmonic expansion up to degree 18 (361 parameters). (b) A three-dimensional view of a spherical B spline used in the lateral expansion of shear velocities. The normalized spline function is localized and axial-symmetric.

caster and Salkauskas, 1990; *Wang and Dahlen*, 1995]. Both Δ and h are in radians. A 3-D view of such a bell-like spline function is shown in Figure 1b. The localized support of these symmetric B spline functions provides effective local control over the lateral features of our model.

2.2. Radial Parameterization

We use 14 cubic B splines distributed nonuniformly to model the radial velocity variations between the Moho surface and the core-mantle boundary (CMB). This leads to a total of $14 \times 362 = 5064$ unknown coefficients. If we define z_i ($i = 1, 2, 3, 4, ...$) as knots, then radial B splines of order n are related to those of order $n-1$ by the following recurrence relation [*Lancaster and Salkauskas*, 1990]:

$$B_{i,n}(x) = \frac{x - z_i}{z_{i+n-1} - z_i} B_{i,n-1}(x) + \frac{z_{i+n} - x}{z_{i+n} - z_{i+1}} B_{i+1,n-1}(x),$$

(3)

where $i = -3, ..., N - 1$ ($N = 3$ for cubic B splines), $n = 1, 2, 3, 4$, and

$$B_{i,1} = \begin{cases} 1, & x_i \le x \le x_{i+1} \\ 0, & \text{otherwise,} \end{cases}$$

(4)

The local support of these B splines not only allows for better control over the radial features, but also leads to faster computation since only neighboring B splines are needed to compute the value at a given point. The derivatives of B splines can be obtained from (3) and (4). We require the second derivatives of the B splines to vanish at both ends; these splines can be asymmetric.

We explore two classes of radial basis functions for the inversion of 3-D shear velocity heterogeneities in the mantle. In the first approach, the mantle is radially parameterized by 14 unevenly distributed B splines. The distribution of the knot locations more or less reflects the radial resolution of the data. The splines span smoothly across the 670-km boundary (shown in Figure 2a), which effectively implies a priori that the velocity perturbations in the mantle are continuous (models obtained using this representation will be referred to as continuous models). The second approach uses two or three sets of B spline functions, split at 670 km and other mantle depths to minimize leakage of the structure from above and below one or more potential boundaries in the mantle due to radial smoothing. In Figure 2b, variations in the upper and lower mantle are described using six and eight B spline functions, respectively. This approach contains higher nominal resolution in the upper mantle than the continuous model and enables us to image potential sharp changes in the velocity variations across 670 km. Models obtained from this approach will be referred to as split models.
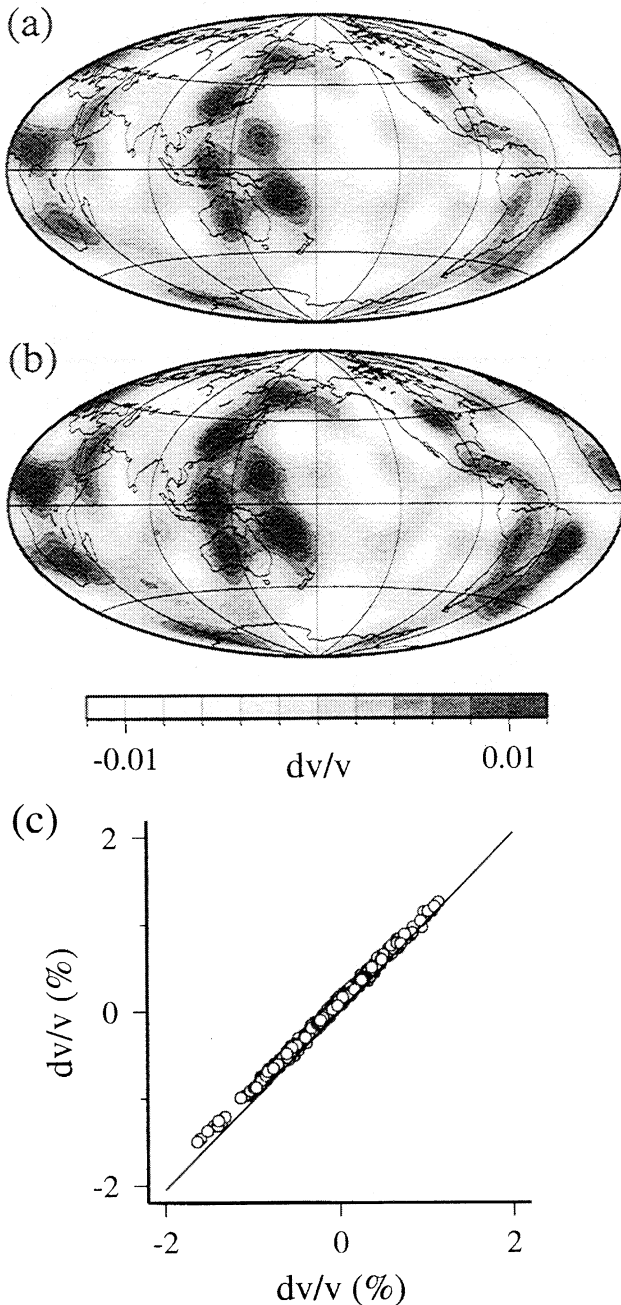
It is important to test the inherent assumptions in the continuous and split parameterizations before the
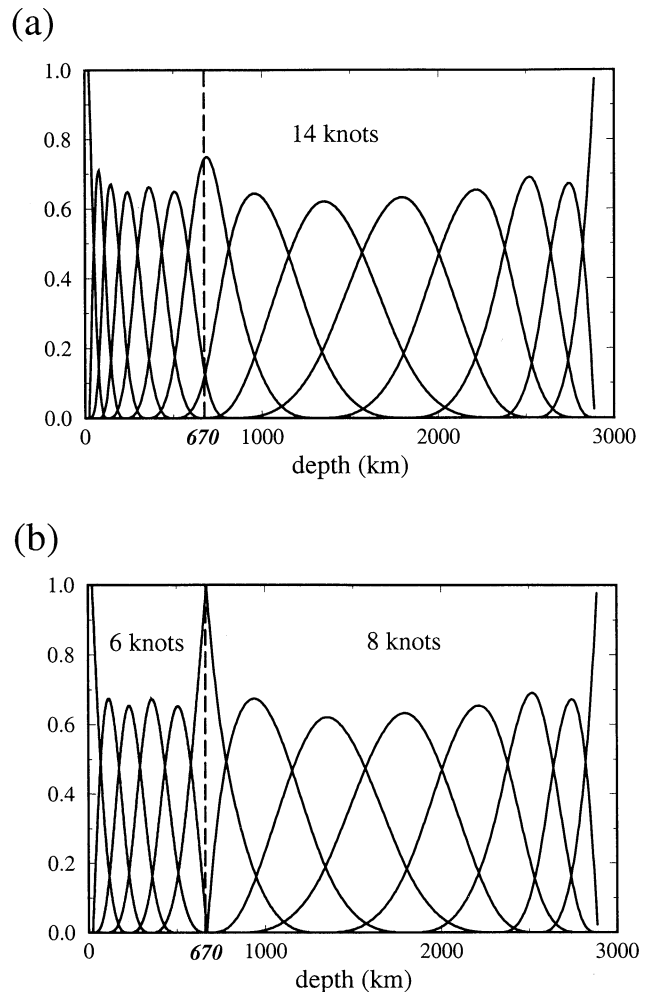
Figure 2. Radial parameterizations for S362C1 and S362D1. We use 14 knots to describe the structure from the Moho surface to the CMB. (a) Continuous radial basis functions of S362C1. One set of B spline functions is used to represent all mantle depths. (b) Split radial basis functions of S362D1. We use two sets of B splines: six for the upper mantle and eight for the lower mantle. This parameterization provides a higher nominal resolution at the 670-km discontinuity.

inversion. We calculate the model predictions of mantle heterogeneity from S12/WM13 [*Su et al.*, 1994] using a grid of densely sampled points in three dimensions. Because S12/WM13 (S12) is a smooth spherical harmonic model with continuous Chebyshev radial basis, the predicted velocity values vary smoothly across the 670-km boundary. We then invert these model values using the continuous and a singly split (at 670 km) B spline parameterizations, respectively, without smoothing. A comparison of these expansions of the shear velocities at 670 km is shown in Figures 3a and 3b. A uniform sampling of velocities at this depth (Figure 3c) shows an excellent correlation in the recovered model values in both cases, with the split parameterization recovering up to 99% of the original peak-to-peak amplitude.

$$\delta t = \sum_k \sum_i C_{ki}\alpha_{ki}, \tag{5}$$

where C_{ki} are unknown coefficient to the expansion of $(\delta v/v)$ in B splines. The 3-D kernel α_{ki} can be calculated from

$$\alpha_{ki} = \int_{(\theta_s,\phi_s)}^{(\theta_r,\phi_r)} G[r(s)]B_k[r(s)]S_i[\theta(s),\phi(s)]\,ds, \tag{6}$$

where

$$G[r(s)] = -\frac{r^2(s)}{v^2 p}. \tag{7}$$

The limits of integration are from the source location to the receiver along the great circle path. S_i represents the ith horizontal spline function, B_k is the radial function defined at the kth knot, and p is the ray parameter.

For surface wave phase velocities and the waveform inversion we replace equation (14) of *Woodhouse and Dziewonski* [1984] by

$$\hat{C}_k = \sum_i \hat{S}_i C_{ki} \tag{8}$$

$$\tilde{C}_k = \sum_i \tilde{S}_i C_{ki}, \tag{9}$$

where $\hat{S}_i$ and $\tilde{S}_i$ are great circle and minor arc path averages, respectively, and are defined as follows:

$$\hat{S}_i = \frac{1}{2\pi}\oint_{\theta_s,\phi_s}^{\theta_r,\phi_r} S_i(\theta,\phi)ds \tag{10}$$

$$\tilde{S}_i = \frac{1}{\Delta}\int_{\theta_s,\phi_s}^{\theta_r,\phi_r} S_i(\theta,\phi)ds. \tag{11}$$

Δ is the arc distance between the source and station. We retain the algorithms of *Woodhouse and Dziewonski* [1984], but parameterized in B splines. Most of the path integrals will be outside the circle in which the spline has nonzero values.

The data from body and mantle wave waveforms are collected from Incorporated Research Institutions for Seismology (IRIS), GEOSCOPE, MEDNET and other seismic networks. The synthetic seismograms are computed from the path average approximation [*Woodhouse and Dziewonski*, 1984]. Potential drawbacks with the approach were discussed by *Li and Romanowicz* [1995]. The use of a large database and a variety of data types in this study, however, help to reduce the errors related to this approximation. S12 is used as the starting model to account for the nonlinear nature of the waveform inversion.

The set of equations for the inverse problem can generally be written in the following form:

$$\mathbf{d} = \mathbf{A}\cdot\mathbf{x} + \mathbf{e}, \tag{12}$$

where $\mathbf{d}$ is a vector of observations, $\mathbf{x}$ is the model vec-

Figure 3. Representations of S12/WM13 [*Su et al.*, 1994] using B splines. The sample maps are the velocity variations at 670 km. (a) B spline parameterization of S12 with continuous radial basis functions across the 670 km (see Figure 2a). (b) B spline parameterization of S12 with discontinuous radial basis functions across the 670 km (see Figure 2b). (c) Correlation of 362 uniformly sampled points between the velocity maps in Figures 3a (x-axis) and 3b (y-axis), plotted in percent perturbations. The solid line represents the case of a perfect correlation.

3. Inversion Methods

To set up the inversion, we express the perturbation in travel times of S, SS, ScS, SKS, and $SKKS$ as

tor, and **e** is the vector of errors. Solutions can only be obtained through iterations and the equation for the final iteration (similar to that of *Su et al.* [1994]) is defined as follows:

$$\delta \mathbf{d}_0 = \mathbf{A}_0 \cdot \delta \mathbf{x}, \tag{13}$$

where $\delta \mathbf{x} = \mathbf{x} - \mathbf{x}_0$, $\delta \mathbf{d}_0$ is the difference between the observation and model prediction for the previous iteration, and $\mathbf{A}_0$ is the respective kernel matrix. In addition to minimizing the deviations between the observations and model predictions, we also choose to minimize the integrated squared gradients of the model. For the final iteration we require

$$|\mathbf{A}_0 \cdot \delta \mathbf{x} - \delta \mathbf{d}_0|^2 + \eta^2 g^2 = \min, \tag{14}$$

where η is a constant weighting factor. The second term in (14) expresses the requirement that the total squared gradient of the model perturbation with respect to the "target" model be minimized; the "target" model in our case is null. The term g^2 is the integrated squared gradient:

$$g^2 = \int_\Omega \int_{r_{\text{bot}}}^{r_{\text{top}}} |\nabla(\delta v / v_0)|^2 dr d\Omega. \tag{15}$$

The limits of integration r_{bot} and r_{top} range between r_{CMB} and r_{Moho}. Differentiation with respect to **x** produces (for the final solution vector **x**)

$$(\mathbf{A}_0^T \cdot \mathbf{A}_0 + \mathbf{D}) \cdot \delta \mathbf{x} = \mathbf{A}_0^T \cdot (\mathbf{d} - \mathbf{A}_0 \cdot \mathbf{x}_0), \tag{16}$$

where $\mathbf{A}_0^T$ represents the transpose of $\mathbf{A}_0$, and **D** is the damping matrix. Because of the different radial and horizontal resolution it is convenient to distinguish between radial and horizontal damping:

$$\mathbf{D} = \gamma_h \mathbf{D}_h + \gamma_r \mathbf{D}_r, \tag{17}$$

where γ_h and γ_r are empirically determined horizontal and radial damping parameters, respectively. Evaluation of the elements of $\mathbf{D}_h$ and $\mathbf{D}_r$ is described in Appendix A. In theory, γ_h and γ_r can be determined on the basis of theoretical considerations if the error of the data sets can be correctly assessed [*Ho-Liu et al.*, 1989]. However, the errors in theory and the likely presence of systematic errors make this an impractical task. The least squares solution to the incremental change in the model $\mathbf{x} - \mathbf{x}_0$ is given by

$$\mathbf{x} - \mathbf{x}_0 = (\mathbf{A}^T \cdot \mathbf{A} + \mathbf{D})^{-1}(\mathbf{A}^T \cdot \mathbf{d} - \mathbf{A}^T \cdot \mathbf{x}_0). \tag{18}$$

The inverse of $(\mathbf{A}^T \cdot \mathbf{A} + \mathbf{D})$ is computed by the Cholesky factorization method [*Trefethen and Bau*, 1997].

4. Data and Data Sensitivity

Three basic data sets are used in our inversions (see Table 1). The first data set consists of absolute travel time measurements of S, SS, ScS, and differential

Table 1. Data Sets Used in Inversions

Data Type	Observations
Absolute Travel Times	
S	26,462
SS	11,410
ScS	4422
Differential Travel Times	
$SS - S$	5124
$ScS - S$	3567
$S - KS$	3550
$SKKS - SKS$	2232
Body and Mantle Waveforms	
Body waves set 1 ($T > 45$ s, V)	4672
Body waves set 1 ($T > 45$ s, T)	3987
Body waves set 2 ($T > 45$ s, V)	1934
Body waves set 2 ($T > 45$ s, T)	1742
Mantle waves ($T > 85$ s, V)	3523
Mantle waves ($T > 85$ s, T)	2840
Mantle waves ($T > 135$ s, V)	3353
Mantle waves ($T > 135$ s, T)	2810
Mantle waves ($T > 200$ s, V)	3470
Mantle waves ($T > 200$ s, T)	1880
Surface Wave Dispersion	
Love wave (35-150 s)	15,473-23,228
Rayleigh wave (35-150 s)	28,457-37,739

Set 1 represents a data set with recordings from 1991–1998; set 2 represents a data set with recordings from 1977–1990; T, period; V, vertical; T, transverse.

travel times of $SS - S$, $S - SKS$, $ScS - S$, and $SKKS - SKS$ (sample ray paths are shown in Figure 4). These measurements were obtained from low-pass-filtered digital seismograms with a dominant period of 20 s. Our data set is similar to that used in the study of *Liu and Dziewonski* [1998]; see their Figures 3, 4, and 7 for data coverage. A well-known advantage of the differential travel time residuals is that the source and station effects are effectively removed.

The second data set includes mantle wave (long-period surface wave) and body wave waveform measurements. Synthetic seismograms used in measuring the phase delays are calculated using the method of *Woodhouse and Dziewonski* [1984, 1989]. Part of the data has been used in previous 3-D Earth structure inversions by *Woodhouse and Dziewonski* [1989], *Su et al.* [1994], and *Ekström and Dziewonski* [1998].

To improve the structure in the upper mantle, particularly the lithosphere and asthenosphere, we include surface wave dispersion measurements of *Ekström et al.* [1997], which consist of Love and Rayleigh waves in the period range of 35–150 s with high lateral resolution. Prior to the inversions, we correct the Love and Rayleigh wave dispersion measurements by subtracting the predicted effect of the crustal model CRUST-5.1
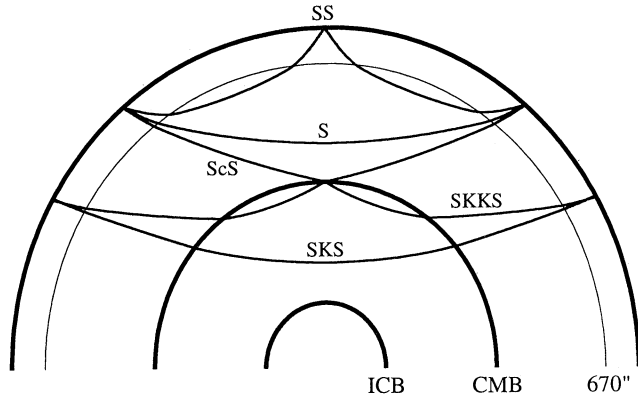
Figure 4. Sample ray paths for the travel time measurements used in this study. The selected epicentral distances are $80°$ for S, ScS, and SS, and $120°$ for SKS and $SKKS$. ICB, inner core boundary; CMB, core-mantle boundary; 670", 670-km discontinuity.

[*Mooney et al.*, 1998]. Travel time data are also corrected for this crustal model, as well as for topography and bathymetry.

Since the data sensitivity to the spline function centered at each radial knot is directly related to the corresponding diagonal elements of the $(\mathbf{A}^T \cdot \mathbf{A})$ maxtrix, we can define a simple normalized diagonal average for each data set to help visualize its contribution in resolving a given basis. For the kth data set and the jth spline, a diagonal element of the horizontally averaged $(\mathbf{A}^T \cdot \mathbf{A})^{(k)}$ matrix is

$$
(\widetilde{A^T A})_{j,j}^{(k)} = \widetilde{\mathbf{V}}_j^{(k)} = \frac{1}{N} \sum_{i=1}^{N} V_{i,j}^{(k)}; \qquad 1 \le j \le M. \quad (19)
$$

N is the total number of horizontal splines, M is the number of radial splines, and $\mathbf{V}$ is a vector containing only the diagonal elements of the $(\mathbf{A}^T \cdot \mathbf{A})$ matrix. This expression represents horizontal averaging of all elements of $\mathbf{V}$ corresponding to the jth radial spline. A graphic representation of the corresponding diagonal elements of the $(\widetilde{\mathbf{A}^T \cdot \mathbf{A}})$ matrices for all the radial B spline functions (labeled in Plate 1a with decreasing depth) is shown in Plate 1b. We compute the contributions of all data sets of this study to the 14 spline functions (normalized to the peak amplitude within each data set). A color-coded representation is shown in Plate 1c. The figure clearly illustrates the varying contribution of different subsets of data to the maximum resolution at various depths. For example, the surface wave dispersion measurements provide the strongest constraints on the structure in the top 200 km; various sets of mantle wave waveforms provide adequate sensitivity in the upper mantle and transition zone, and body wave waveforms provide sensitivity at mid-mantle depths. The absolute travel time measurements help to constrain the structure from immediately below the 670-km discontinuity to mid-mantle depths, whereas

the differential travel times of $S - SKS$, $ScS - S$, and $SKKS - SKS$ are particularly sensitive to the lowermost mantle. It should be noted from Plate 1 that there will always exist a significant discrepancy between the resolution for S and P velocities; the uppermost mantle is mainly controlled by fundamental mode surface waves, which have $\sim 90\%$ energy in shear.

The final $(\mathbf{A}^T \cdot \mathbf{A})$ matrix of (18) is obtained by computing a weighted sum of the $(\mathbf{A}^T \cdot \mathbf{A})$ matrices for the individual subsets of data:

$$
\mathbf{A}^T \cdot \mathbf{A} = \sum_{k=1}^{K} w_k (\mathbf{A}^T \cdot \mathbf{A})^{(k)}, \quad (20)
$$

where the weights w_k are chosen according to the resolving properties of the kth subset of data, its size, and the measurement errors. K is the total number of data sets used in the inversion. Using the two radial parameterizations shown in Figure 2, we obtain a continuous model S362C1 and a discontinuous model S362D1.

5. Possible Mantle Layering

Over the years, many mantle discontinuities have been proposed. Of these, only the 400- and 670-km discontinuities are confirmed by systematic, global observations of reflected and converted phases. Their sharpness is documented through reflections and conversions of incident waves. The phase transformations corresponding to these discontinuities are rather well understood. There have been suggestions of two additional discontinuities in the lower mantle, at ~ 1000 km and 1800 km depths. Since there is no clear evidence of potential phase changes, these would have to be compositional in nature and would have, potentially, a major impact on mantle flow. We investigate each of these four discontinuities with our seismological data set, but focus primarily on the 670-km discontinuity, long suspected of being a chemical or mechanical barrier to mantle flow.

5.1. Shear Velocities Away From 670 km

The best fit models from our inversions predict significant, large-scale heterogeneous structures throughout the mantle. For brevity, we will only show the split model (S362D1, Plate 2) at depths away from the 670-km discontinuity since at these depths it is well correlated with the continuous model (S362C1). At 100 km, shear velocity variations exceeding $\pm 6\%$, with pronounced contrasts between stable continents and mid-ocean ridges, are needed to satisfy the long-period mantle wave waveform and surface wave dispersion observations. The largest positive and negative anomalies are observed under the Canadian Shield and East Pacific Rise, respectively. This is consistent with other published 3-D models of the Earth [e.g., *Su et al.*, 1994; *Masters et al.*, 1996; *Li and Romanowicz*, 1996; *Grand et al.*, 1997; *Ekström and Dziewonski*, 1998]. In general,

the higher velocities under the old oceanic lithosphere due to the cooling of oceanic lithosphere and slow back arc regions are also well captured. The effect related to surface tectonics extends to ~300 km or deeper, shown by the model predictions at 300 km. At 900 km the velocity map is dominated by shorter wavelength variations. The correspondence between the high-velocity anomalies and known region of major downwelling is not complete. There are high velocity anomalies that do not coincide with locations of subduction zones during the last 200 Myr.

At mid-mantle depths our models show large-scale high-velocity anomalies in central Asia, which extend nearly linearly to Tonga-Fiji islands. This feature has been associated with remains of cold slab material from subduction which took place more than 100 Myr ago [*Woodhouse and Dziewonski*, 1989; *van der Hilst et al.*, 1997]. Also present in the model are fast velocity anomalies under Central America and the Pacific. In the bottom 1000 km, coherent slow velocities begin to develop in the center of the Pacific and Africa. Near the CMB, the pattern of heterogeneity is dominated by these two slow velocity regions (equatorial Pacific plume group and great African plume, [*Dziewonski et al.*, 1991, 1993]) and a fast velocity ring under the circum-Pacific [*Dziewonski*, 1984]. These heterogeneities have been associated with pronounced thermal and compositional variations at the base of the mantle [*Wysession et al.*, 1992; *Liu and Dziewonski*, 1998]. Thus our modeling approach using B splines clearly resolves some of the most robust long-wavelength features in the mantle.

5.2. Shear Velocities Near 670 km

One of the main goals of this study is to investigate, using seismological data, the degree to which the large-scale flow is stratified by mineral phase changes or composition across the 670-km discontinuity. Plate 3 shows a comparison of S362C1 (continuous) and S362D1 (split at 670 km) for the structure between 550 and 790 km. At 550 km, both models show consistent large-scale high-velocity anomalies that can be related to subduction in the western and southwestern Pacific. There is also a broad anomaly extending from South America to western Africa. These anomalies span thousands of kilometers laterally. Most of the Pacific ocean and Eurasia show velocities slower than PREM [*Dziewonski and Anderson*, 1981] by ~1%. At 650 km the differences between these two models become significant. Although the continuous model still shows an overall pattern similar to that in the middle of the transition zone, the lateral extent and amplitudes of the major anomalies are less pronounced; a fast anomaly appears under the East Pacific Rise. The heterogeneous structure imaged by this model essentially remains unchanged from above to below the 670-km boundary, as expected, owing to the continuous radial parameterization. Like the continuous model, the split model (Plates 3e–3h) shows

relatively little change in the overall heterogeneities between 550 and 650 km. Below the 670-km discontinuity (at 690 km), however, the long-wavelength high velocities related to subduction in the western Pacific and South America are significantly attenuated. In addition, the weak fast velocities under most parts of the Atlantic are replaced by slower than average velocities. Smaller-scale fast velocities begin to develop in the central Pacific. At 790 km depth the two classes of models return to nearly perfect correlation in the main features. Additional features that are not clearly related to subduction zones, e.g., large-scale fast velocity anomalies under the eastern Pacific, are present in both models at this depth.

We perform resolution tests to examine how well the large-scale features can be resolved using the parameterizations shown in Figure 2a (continuous) and Figure 2b (split). We adopt the same weights for the data sets and same overall smoothing criteria as those used in deriving the final models. A simple input model is shown in Plate 4a with an abrupt velocity change across the 670-km discontinuity; there is a high-velocity anomaly in the Philippines and a low-velocity anomaly in the Pacific lower mantle, and these anomalies extend down to ~1200 km. Inversion using the continuous parameterization recovers ~50% of the peak input amplitude near 670 km; this is significantly lower than the 75% recovered by the split parameterization. This discrepancy directly reflects the higher nominal radial resolutions in the split parameterization near 670 km. The choice of a split parameterization also significantly limits the extent of velocity leakage from lower to upper mantle. The depth-dependent root-mean-squared (RMS) amplitudes of the input and output models are shown in Plate 4b: an inversion using the split parameterization recovers the shape and amplitudes of the RMS of the input model well, while a greater degree of broadening is observed in the case of the continuous parameterization. Both output models, however, correctly recover the peak location of the main anomalies. In addition, inversions using both parameterizations show excellent agreement in the RMS amplitudes with the input model at depths some 150 km away from the main anomalies. This implies that velocity anomalies at depths 150–200 km from the 670-km discontinuity, with lateral and radial dimensions similar to those of this test, can be reasonably well resolved by the data sets and method of this study. Further resolution tests indicate that inversions using these two parameterizations can accurately resolve a simple velocity structure generated by a nonzero, degree 11 spherical harmonic.

With current data sets, however, we cannot determine unequivocally whether the sharp radial change of velocity between 550 km and 790 km (see Plate 3) takes place in a continuous fashion, described by the continuous model, or in a discontinuous fashion, described by the split model. Because of the presence of a major seis-
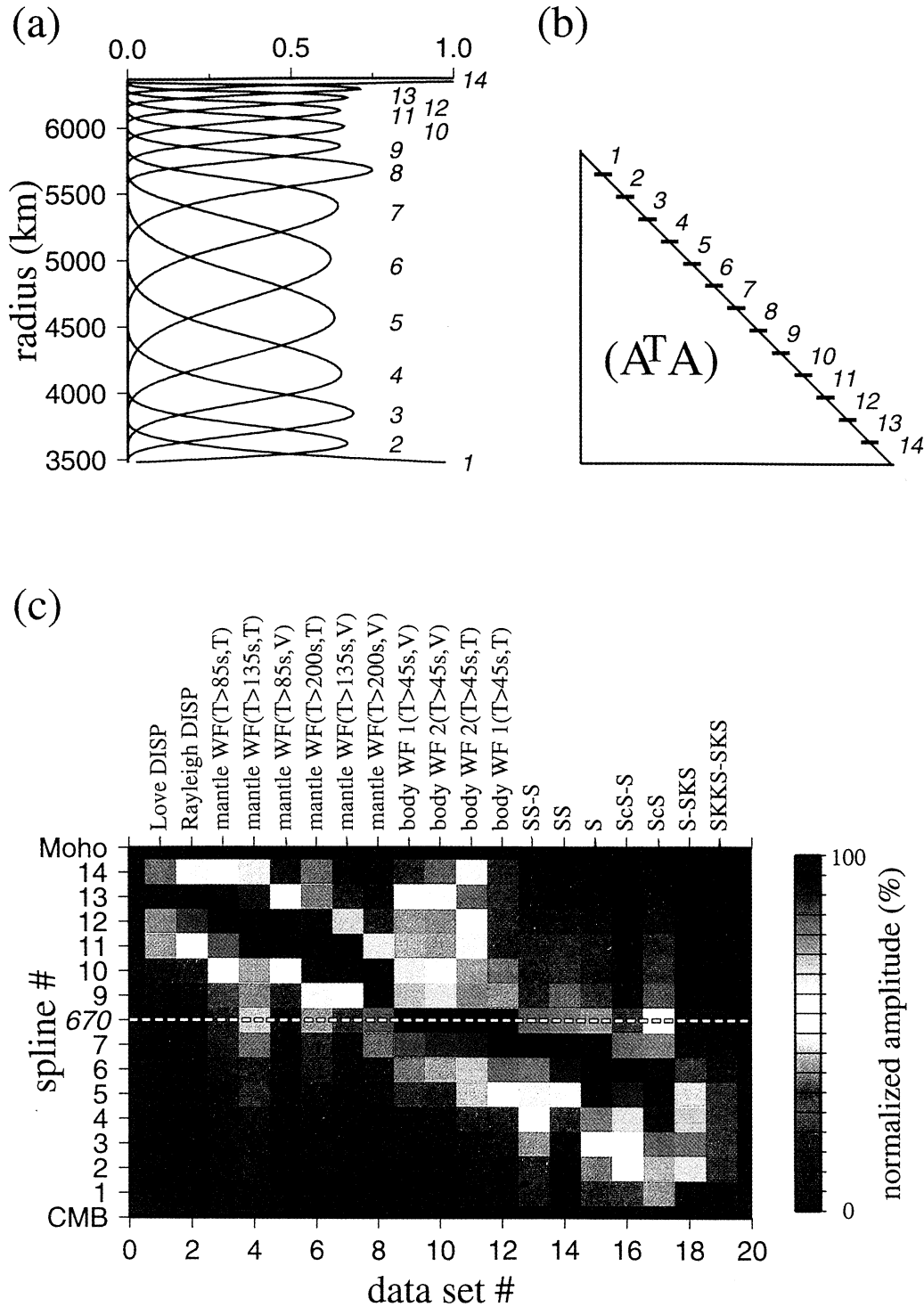
Plate 1. Sensitivity of individual data sets to the 14 spline functions. (a) B splines labeled from the CMB to the top of the mantle for the continuous model parameterization. (b) A graphic representation of the lower half of an $(A^T \cdot A)$ matrix generated by a data set. Numbers 1, 2, ..., 14 and the corresponding segments (as marked) represent portions of the diagonal elements of an $(A^T \cdot A)$ matrix which have the largest contribution to the respective B spline functions. (c) Normalized sensitivity of the data set in resolving the 14 B spline functions (see section 4 for details). The largest sensitivity is shown in dark red. It is clear that the surface wave dispersion measurements are highly sensitive to the near-surface splines. The mantle wave waveforms are sensitive to the upper mantle structure, while body wave waveform and travel time measurements have the largest contributions to depths below 500 km. WF 1 represents a waveform data set with recordings between 1991 and 1998; WF 2 represents a waveform data set with recordings between 1977 and 1990.
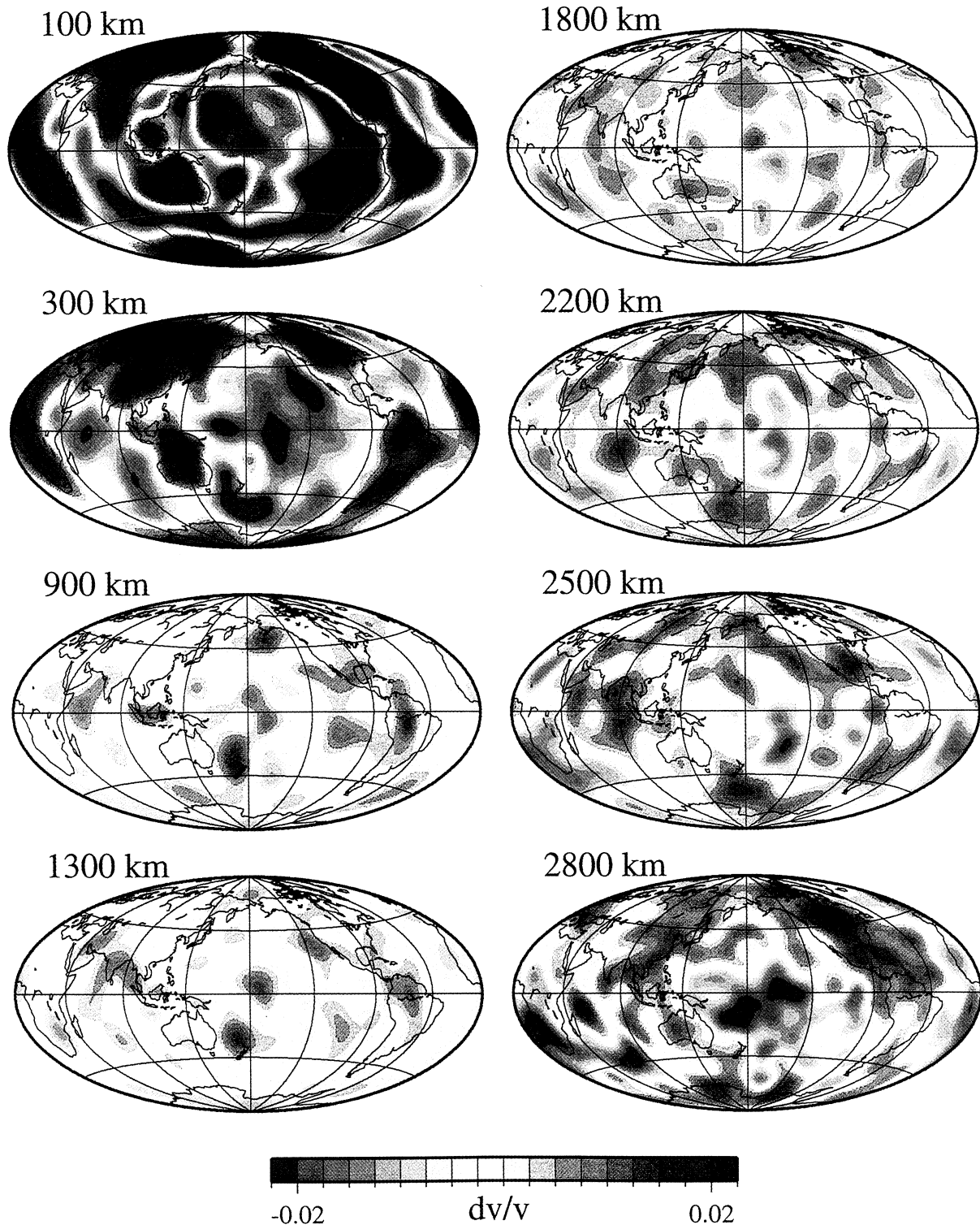
Plate 2. Shear velocity perturbation, predicted by S362D1, at mantle depths away from the 670-km discontinuity. Red represents slower velocities and blue represents faster velocities than those of PREM. Velocity variations over 6% (with a pronounced contrast between stable continents and young oceans) are observed at 100 km, and the effect of surface tectonics persists down to the depth of 300 km. At mid-mantle depths, the velocities are dominated by a linear, fast velocity structure across Asia. The patterns in the bottom 1000 km are dominated by large-scale low velocities under the central Pacific and Africa.
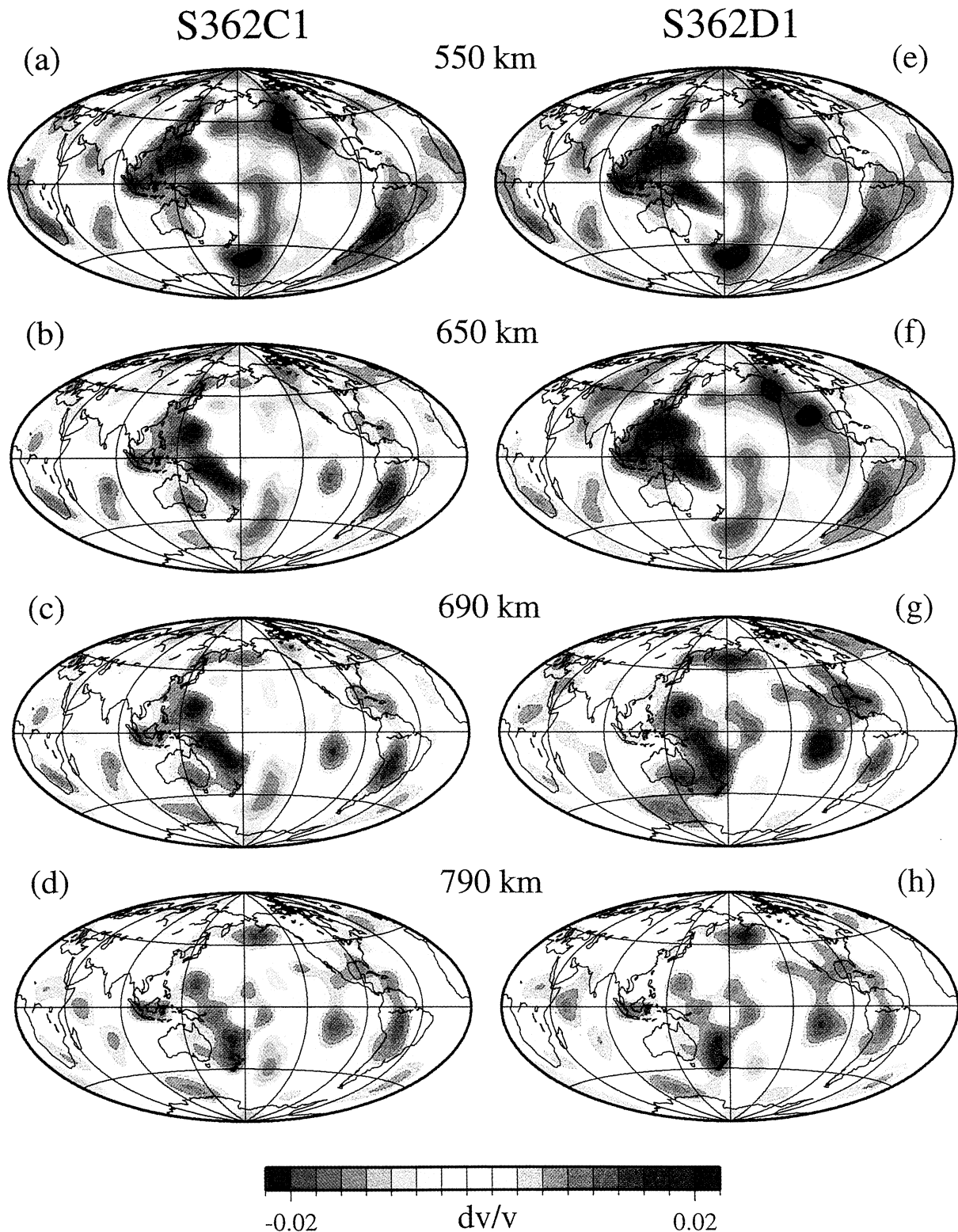
Plate 3. Shear velocity perturbations near the 670-km discontinuity. (a)–(d) Velocity maps predicted by S362C1 (continuous) for 550, 650, 690 and 790 km, respectively. (e)–(h) Velocity maps predicted by S362D1 (split at 670 km) for 550, 650, 690 and 790 km, respectively. The model predictions agree very well at 550 km and 790 km, but significant differences exist closer to 670 km. A significantly greater radial change is observed between the upper and lower mantle in the split model. Both models, however, appear to favor a change of flow pattern, as the dominant structures in the transition zone, e.g., in the Pacific and the southern Atlantic, differ significantly in amplitude and length scale from those in the lower mantle.

(a)

(b)
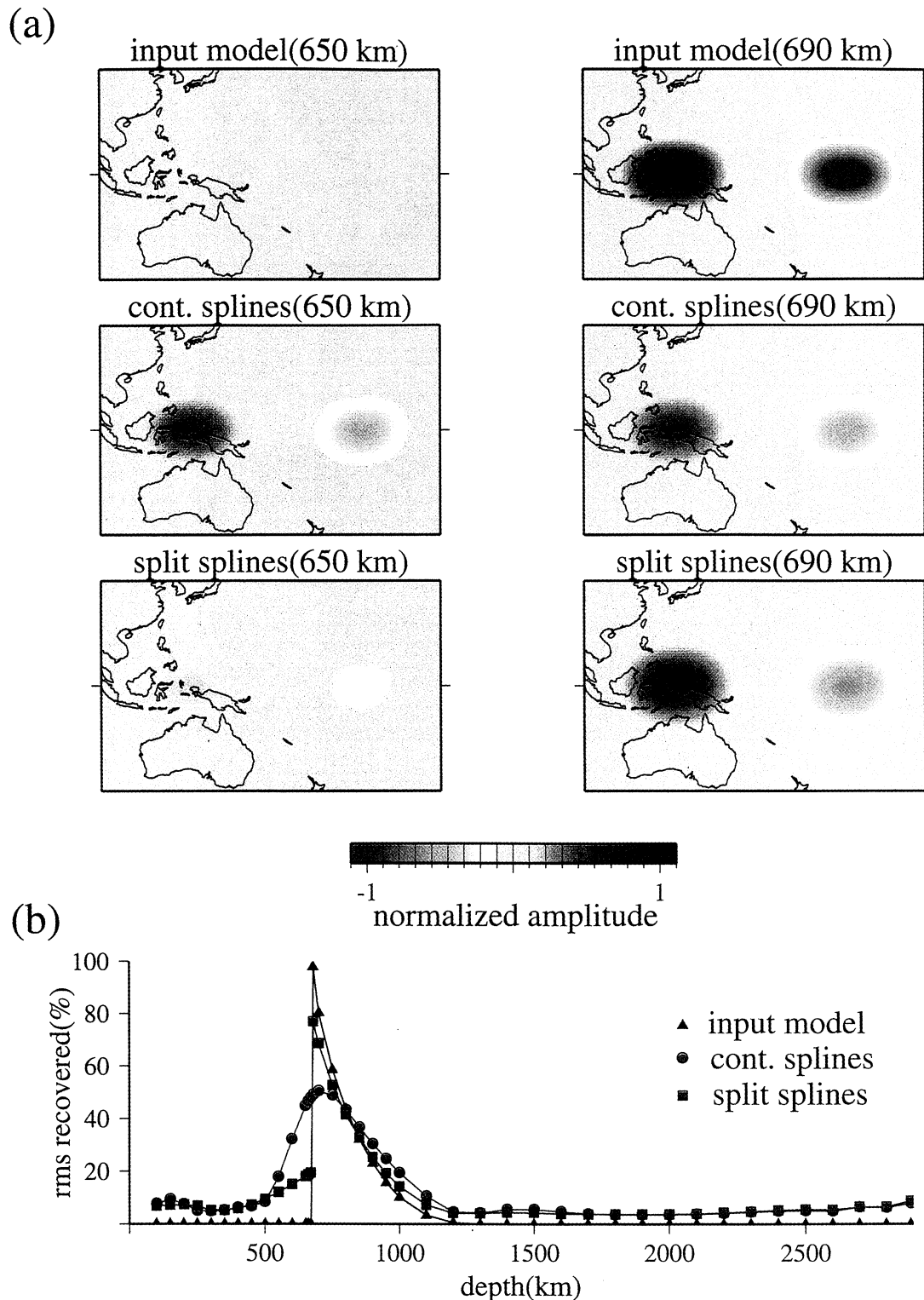
Plate 4. (a) A simple input "blobby" model with a high-velocity anomaly in the western Pacific and a slow anomaly in the central Pacific. Rays are shot through the input model and inversions using the same weights for each data set and the same smoothing criteria are performed to recover the model. The recovered maps using the continuous (see Figure 2a) and split (see Figure 2b) parameterizations are as labeled. Inversions using the split parameterization recover over 80% of the amplitude while introducing little artifact. (b) Root-mean-square amplitude of the heterogeneities of the input and recovered models. The split model is clearly the better model, in this experiment, in retrieving the peak amplitude near 670 km and the radial variation of velocities of the input model throughout the mantle.
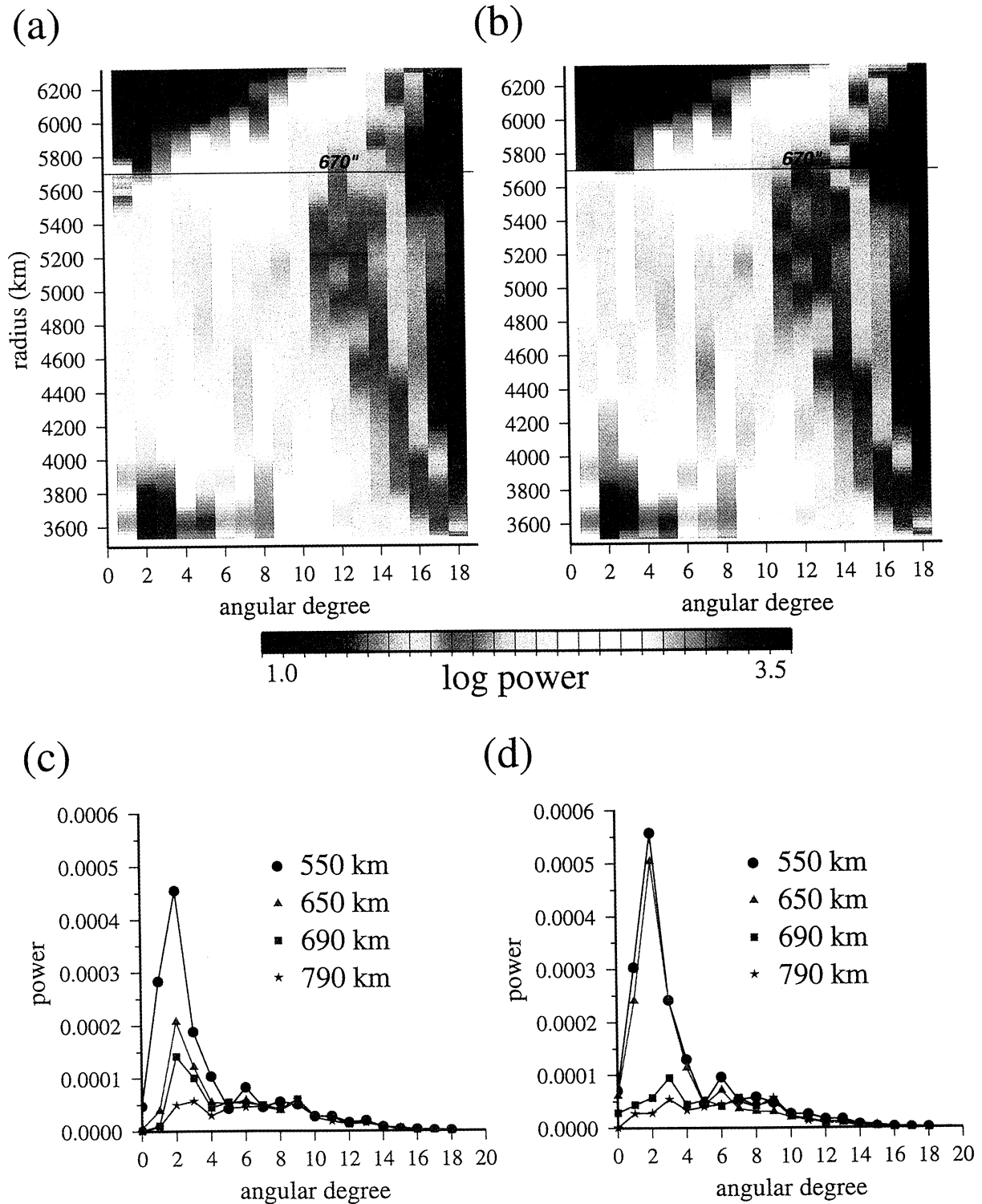
Plate 5. Spherical harmonic power spectra of the velocity maps predicted by (a) the continuous model S362C1 and (b) the split model S362D1. Each color represents a value of $\log_{10}$(power) for a given angular degree at a particular depth. The upper mantle and the lowermost mantle are dominated by low-degree harmonics. (c) and (d) Power spectra for velocity maps at 550 km, 650 km, 690 km and 790 km, plotted on a linear scale. In both S362C1 (Plate 5c) and S362D1 (Plate 5d) a pronounced degree 2 signature in the upper mantle becomes nearly white in the lower mantle, suggesting a change in the flow pattern or composition between these two regimes.

mic discontinuity and potentially sharp changes of other elastic and anelastic properties near 670 km, it is natural to assume an abrupt change in flow pattern rather than a steep change in the velocity gradient to explain this significant radial variation in velocity. However, as stated in section 1, we demonstrate here the existence, not uniqueness, of a model with a radial discontinuity in the pattern of lateral heterogeneity.

5.3. Variation of Power Spectra

Plate 5 compares the spherical harmonic power spectra of S362C1 and S362D1 as a function of depth. At each sampled depth the velocity variations are expanded to spherical harmonics up to degree 18. Near the surface, velocities predicted by these two models are dominated by degree 1 and 5 spherical harmonics. This is consistent with earlier shear velocity models [*Su and Dziewonski*, 1991], and is related to the seismic signatures resulting from the continent-ocean contrast. A gradual decrease of degrees 3, 4 and 5 is visible below 350 km, where heterogeneities related to the deep roots of continents becomes less pronounced. There is a clear cutoff in the amplitude of the low-degree harmonics immediately beneath the transition zone. This change in the spectrum is abrupt in the case of the split model at 670 km, but it is distributed over 200 km in the case of the continuous model. The spectrum is nearly white between 800 and 1800 km (only weak degree 3 and degree 6 harmonics are present); below 1800 km, lower-degree harmonics, degree 2 in particular, once again become dominant.

Plates 5c and 5d show the power spectra at the respective depths of Plate 3 on a linear scale. In both cases, a clear transition from a red spectrum to nearly white in 250 km is evident: at 550 km, both models show a pronounced degree 2 signature; at 790 km, however, the degree 2 amplitude falls below one fifth of the the amplitude in the center of the transition zone. The low power in the models between 790 and 1750 km is well resolved, as most of the travel time data observations have high sensitivity in this depth range. This observation is consistent with the recent findings of *Liu* [1997], in which it is associated with a possible change of the mantle flow pattern. An increase in the low-degree signature at 1750 km coincides with the location of a possible horizontal impedance layer inferred from seismic [*van der Hilst and Kárason*, 1999] and flow calculations [*Kellogg et al.*, 1999], but the change is gradual, with the overall power steadily increases toward the CMB. This transition and the spectral falloff between 550 km and 770 km correlate well with the important features in the "avalanche" model of *Tackley et al.* [1993] (see their Figure 5, which shows a red spectrum in the transition zone due to accumulation of subducting material, a low-amplitude, white spectrum, at mid-mantle depths, and a red spectrum near the base of the mantle due to "splattering" of the avalanches).
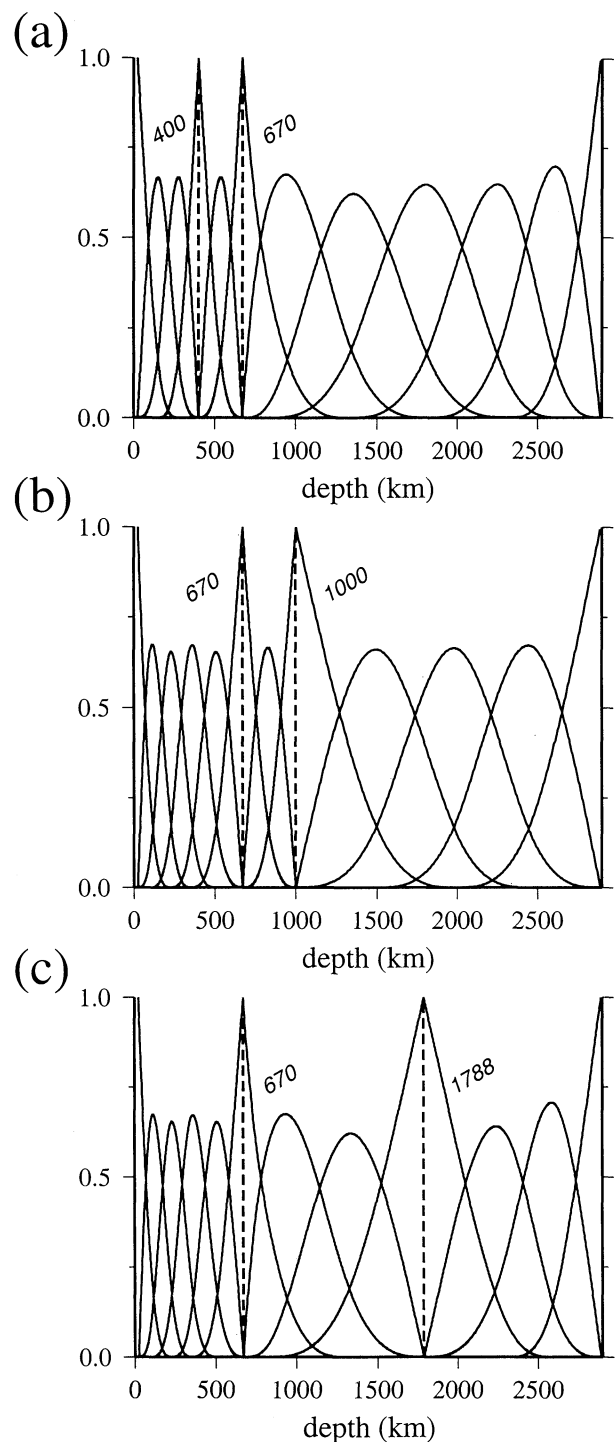

Figure 5. Radial basis functions for a model with (a) discontinuous parameterizations at 400 and 670 km, (b) discontinuous parameterizations at 670 and 1000 km, and (c) discontinuous parameterizations at 670 and 1788 km. Inversions using these parameterizations allow shear velocities to vary discontinuously across 400, 1000 and 1788 km, respectively, in addition to 670 km.

5.4. Other Possible Discontinuities

It is important to examine other possible indications of flow pattern changes in the mantle, resulting either from phase transformations (e.g., at 400 km) or com-
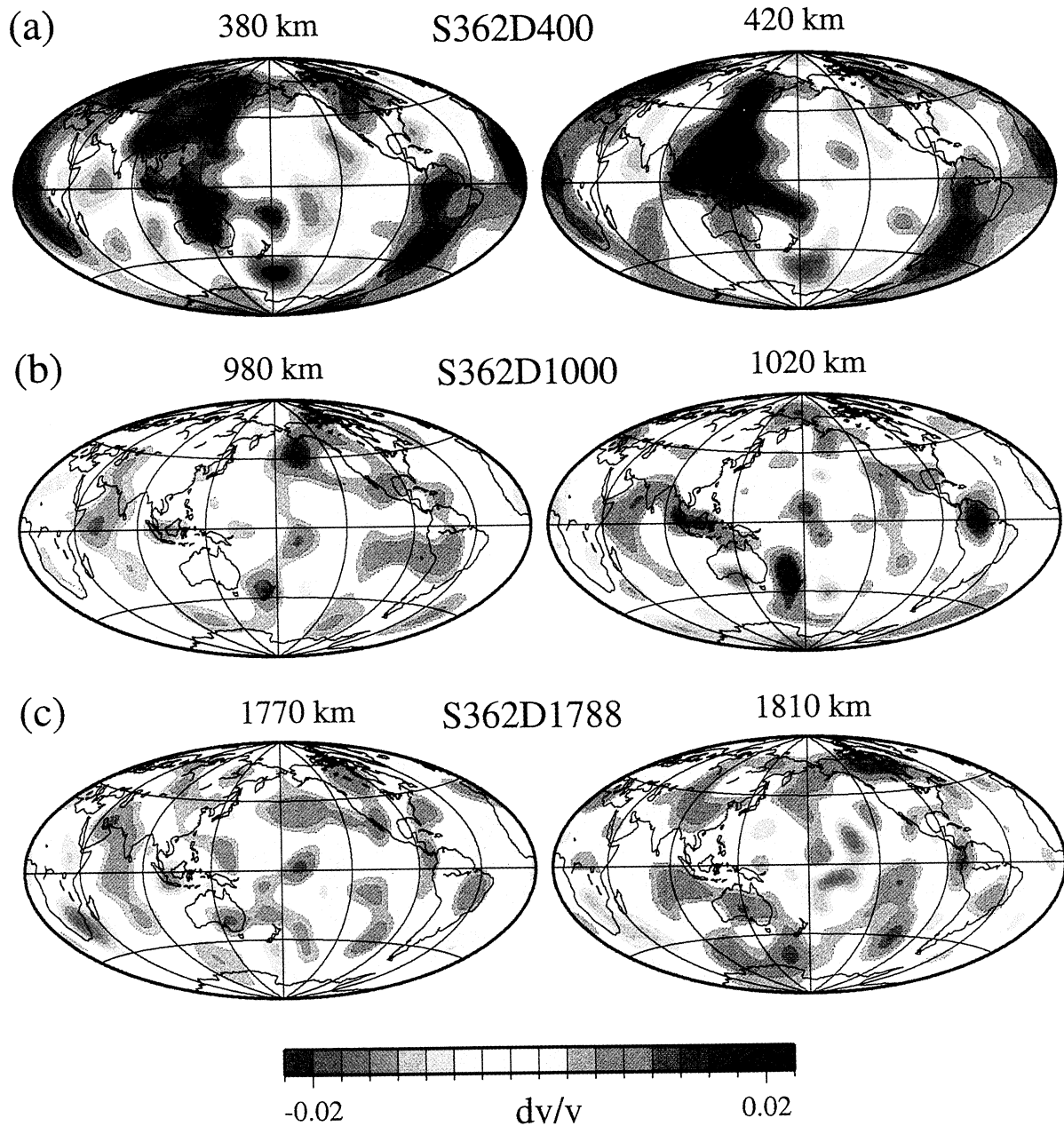
Plate 6. Model comparison for depths near the proposed mantle discontinuities for radial basis shown in Figures 5a to 5c, respectively. The slices are taken from shear velocity structures: (a) near 400 km for inversions using radial basis shown in Figure 5a, (b) near 1000 km for inversions using radial basis shown in Figure 5b, and (c) near 1788 km for inversions using radial basis shown in Figure 5c.
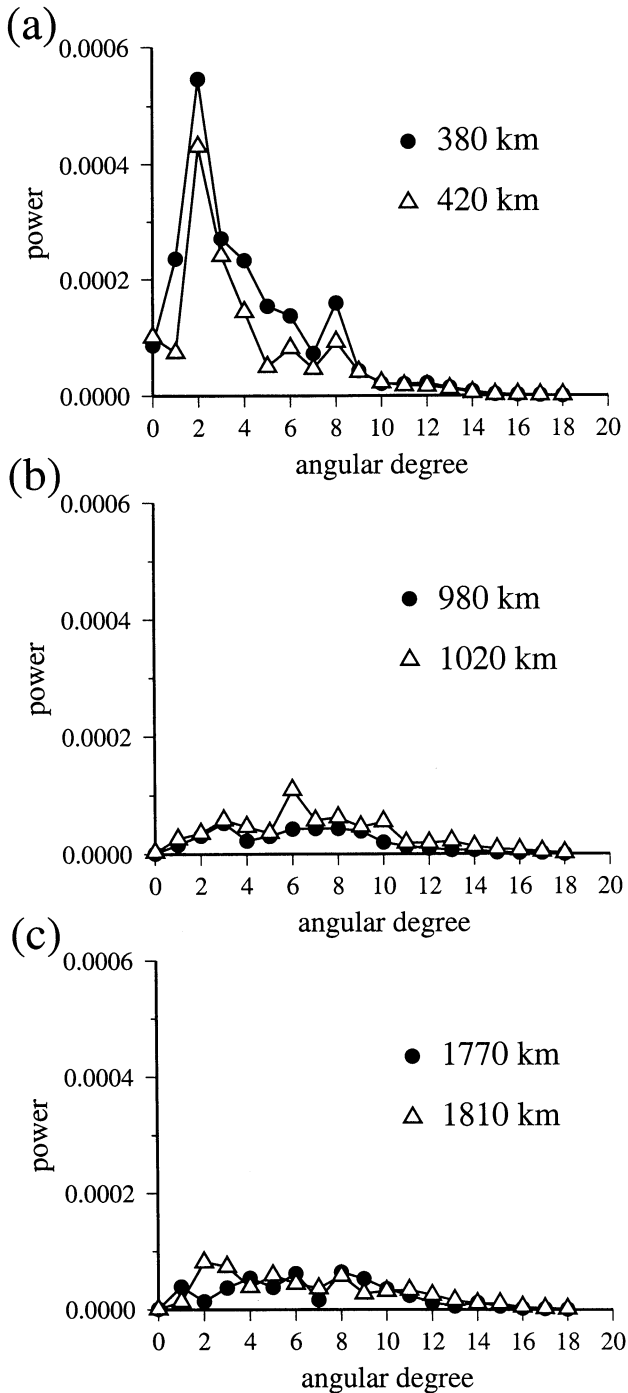
Figure 6. Power spectra (plotted on a linear scale) near (a) 400 km, predicted by S362D400, (b) 1000 km, predicted by S362D1000, and (c) 1788 km, predicted by S362D1788. The power spectral differences above and below these potential boundaries are generally small. S362D1788 shows a modest increase of degree 2 signature.
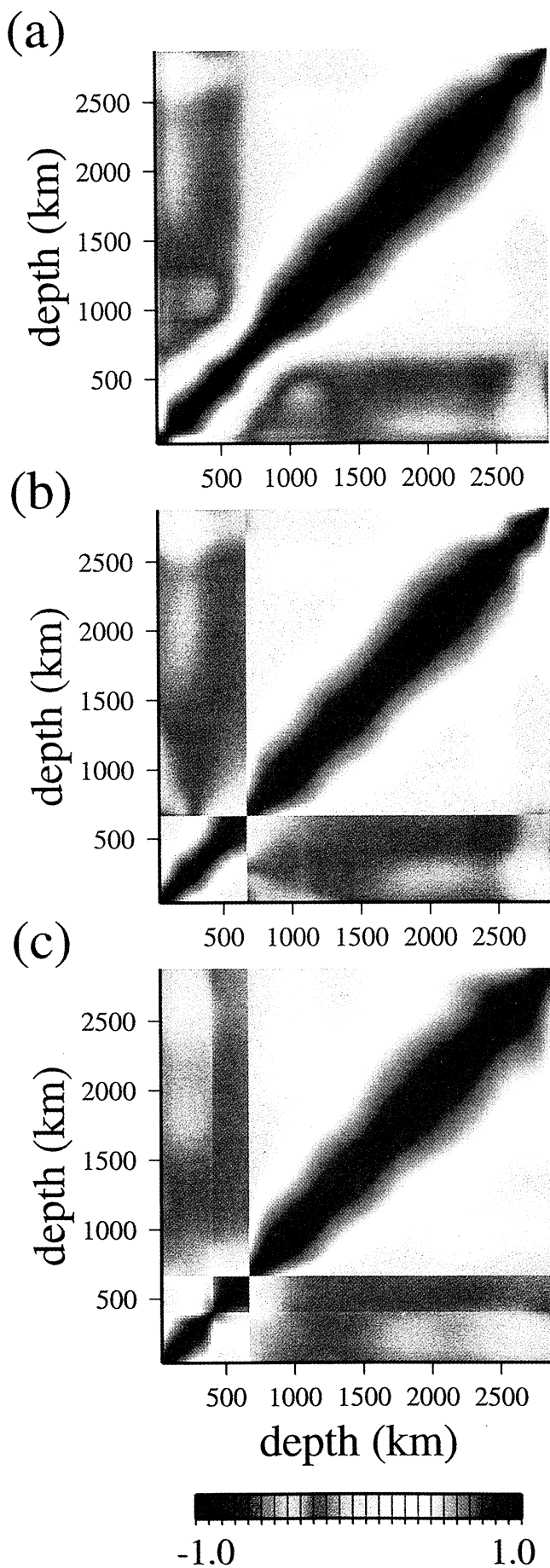
positional changes, particularly at depths where models S362C1 and S362D1 (see Plate 5) predict notable changes in the power spectra. In some cases, these changes appear to take place over a few hundred kilometers, e.g., near 1800 km. These "gradual" changes may not be well resolved from our previous experiments, since the radial parameterizations so far do not per-

mit the velocity to vary freely above and below a given depth, other than at 670 km in S362D1; effectively, the inversion results are likely to be biased toward smooth variations. To account for this deficiency, we perform inversions with a discontinuous radial parameterization at 400, 1000 and 1788 km (Figure 5). Radial changes in shear velocities across these proposed boundaries could potentially reflect flow changes at the corresponding depths.

The seismic discontinuity at 400 km has been widely associated with an exothermic phase transition of olivine from α to β phase. Potentially, this transition can have significant impact on the convective flow in the upper mantle. We perform inversions using a radial parameterization shown in Figure 5a and two slices through the best fit model (S362D400, split) are shown in Plate 6a. This model shows continuity of fast velocities across 400 km beneath South America and Africa and of slow velocities under the southern Pacific and the Indian Ocean. The amplitudes of some of these anomalies are slightly reduced below 400 km. The most significant difference is a notable eastward shift in the large-scale fast regions from beneath central Eurasia to the western Pacific subduction zone. The fast velocities associated with the Australian shield is much attenuated in the transition zone. These features signal a relatively smooth transition from a predominantly continent-ocean signature in the top mantle to a subduction driven process in the transition zone. The continuity of the structure demonstrates that our inversions are robust and that results are only marginally affected by a discontinuous model parameterization. The linear power spectra of the best fit model at 380 and 420 km (Figure 6a) agree well with those of S362D1 in the upper mantle. There is a considerable drop-off in the amplitudes of degree 1, 4, 5, and 7 and a modest decrease in degree 2 and 3 in the transition zone.

Recent studies of mantle secondary phases [e.g., *Peterson et al.*, 1993; *Kawakatsu and Niu*, 1994, 1996] and heat flux [*Forte and Woodward*, 1997] suggest a possible change of mantle flow near 1000 km. Our modeling so far has shown little evidence for an abrupt change in the long-wavelength shear velocity variations near this depth. We extend the analysis by allowing the velocities to vary discontinuously across a boundary at 1000 km (see Figure 5b). The maps at 980 and 1020 km (Plate 6b) display a good overall correlation in the large-scale features. Differences are mostly in amplitudes of major anomalies, e.g., near northern part of South America, the Philippines and New Zealand. The sampled power spectra (Figure 6b) for the best fit model from the inversion are nearly white above and below 1000 km; only a modest increase in degree 6 and 10 is present. The radial coherence in the main velocity patterns and power spectral signature suggests that a significant change in flow near 1000 km is not required by the data used in our inversions.

Recently, *van der Hilst and Kárason* [1999] suggested that a compositional heterogeneity may exist in the

(a)

depth (km)

500 1000 1500 2000 2500

(b)

depth (km)

500 1000 1500 2000 2500

(c)

depth (km)

500 1000 1500 2000 2500

depth (km)

-1.0   1.0

bottom 1000 km of the Earth's mantle. Earlier tomographic models [e.g., *Dziewonski and Su*, 1993; *Su et al.*, 1994] observed an increase in the spectral power of low-degree harmonics in the lower 1000 km, similar to that of S362D1 (see Plate 5). Model predictions at 1770 km and 1810 km from inversions using a radial basis with two discontinuities (S362D1788, see Figure 5c for radial parameterization) are shown in Plate 6c. The length scale of most velocity features at these two depths is much shorter than those in the upper mantle or lowermost mantle. There are some weak indications of the development of the "Pacific superplume" and fast velocity belt around the Pacific below 1800 km. The model does not contain a dominating signal in the power spectral content (Figure 6c) at depths above 1788 km, similar to that at 1000 km; this reflects the complexity of the velocity structure. Although a sharp change of flow is not supported by this model, relative radial variations above and below 1800 km are somewhat larger than those at 1000 km, both in the amplitude and locations of major anomalies and in a moderate increase in the degree 2 signature. This, however, may be explained by the proximity of the CMB, which would force the vertical flow to become horizontal.

5.5. Radial Correlations and Power Spectra

The radial correlation function [*Jordan et al.*, 1993] for the continuous model S362C1 (Plate 7a) shows a change in the width of the band of high correlations along the diagonal; there is a slight narrowing close to 670 km before the width increases substantially in the lower mantle. Much of this variation could be attributed to the change in the spacing of the radial B splines. Since a continuity condition is imposed, there cannot be a total decorrelation between the upper and lower mantle. Such decorrelation, however, is observed in the split model S362D1 (see Plate 7b), where there is an abrupt change at the discontinuity. An important feature common to both models is a transition from positive to negative correlation in the proximity of 670 km (color-coded by a red to green transition), which indicates a change of pattern in the velocity structure between the transition zone and the lower

Plate 7. Radial correlation functions [see *Jordan et al.*, 1993] for (a) continuous model S362C1, (b) split model S362D1, and (c) model S362D400. Present in Plates 7a and 7b are a change in the width of the diagonal and a transition from positive to negative correlation in the proximity of 670 km (color-coded by a red to green transition) near 670 km. However, no significant transition is present near 400 km, shown by a strongly positive correlation (red contour) at adjacent depths. The difference in the radial correlations between 670 and 400 km (Plate 7c) implies a significantly smaller radial change at 400 km in comparison with that at 670 km.
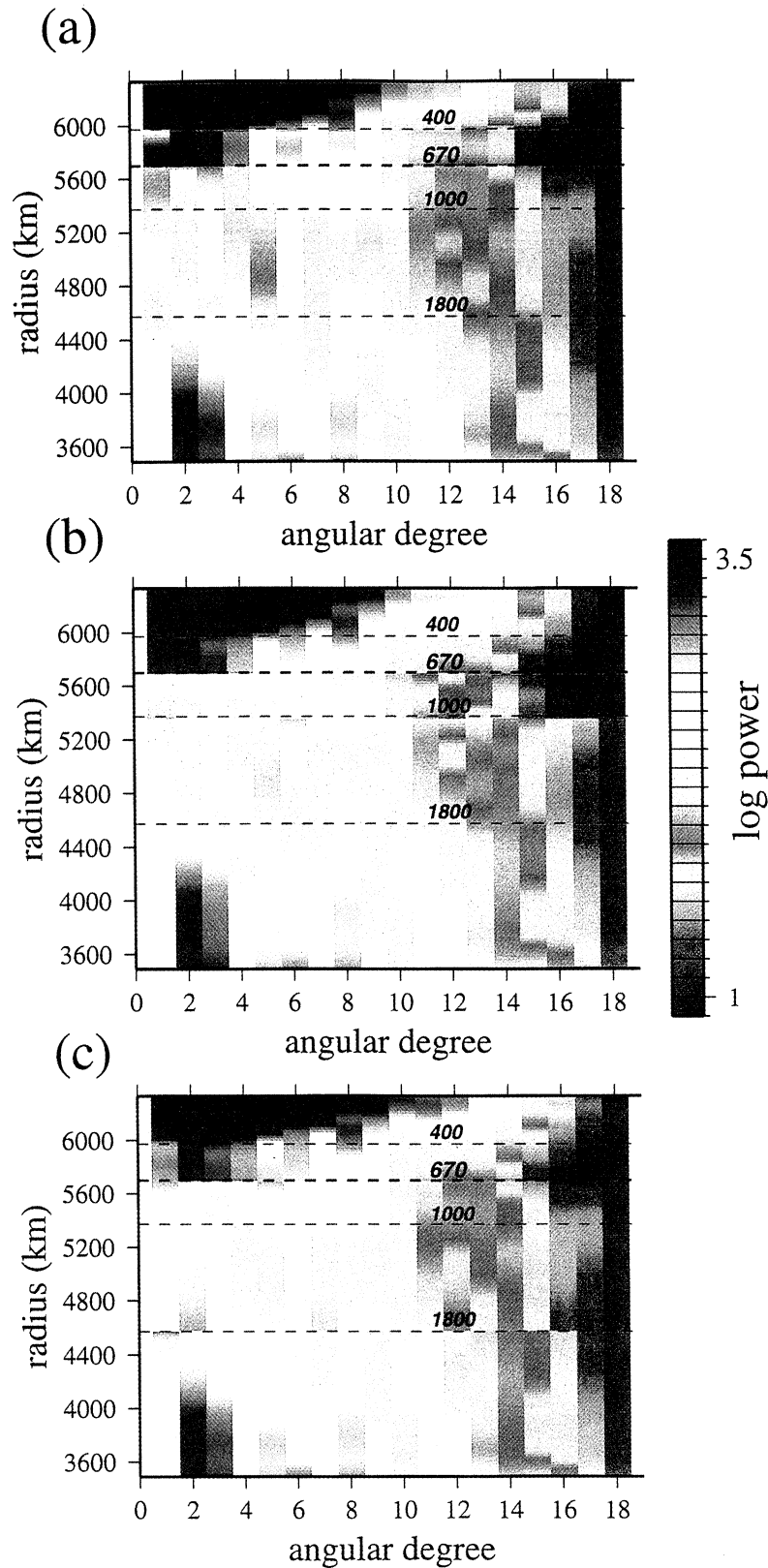
Plate 8. Spherical harmonic power spectra of the velocity maps predicted by three split models. Definition of colors are the same as those of Plate 5. (a) Power spectra of S362D400, with discontinuous radial basis at 670 and 400 km. (b) Power spectra of S362D1000, with discontinuous radial basis at 670 and 1000 km. (c) Power spectra of S362D1788, with discontinuous radial basis at 670 and 1788 km. All three models show high spectral amplitude in lower-degree harmonics in the lithosphere and the lowermost mantle. Little change is visible near 400 and 1000 km, and only a modest change is present near 1800 km.

mantle. Plate 7c shows the radial correlation function of S362D400 (parameterized discontinuously at 400 and 670 km). The overall characteristics near 670 km are in excellent agreement with those of S362D1 (see Plate 7b). Both models contain a significant decorrelation/anticorrelation between the structures above and below 670 km. However, no notable transition is present near 400 km, shown by a strongly positive correlation (shown in red) at adjacent depths, despite the addition of free parameters introduced by the model parameterization of S362D400 at this depth. The difference in the radial correlations between 670 and 400 km in Plate 7c implies a much weaker radial change at 400 km in comparison with that at 670 km.

In general, even though the radial correlation function is frequently used to assess the continuity of flow, it is not as effective in detecting changes in the pattern of heterogeneity as monitoring of the power spectra. For example, a profound change in the dominating wavelength of heterogeneity between the upper and lower mantle is clearly evident in Plate 5, while there is a much weaker indication of it in Plate 7.

Logarithmic power spectra of models of multiple discontinuities (Plate 8) generally show high correlation with those of S362D1 (see Plate 5b), though modest differences arise close to the splitting depths. The agreement implies that the artifacts introduced by the split model parameterizations are generally small. It is evident that the choice of radial parameterizations has little effect on the dominant low-degree signatures in the upper mantle and near the CMB. Our experiments on the radial variations suggest that in addition to a 670-km discontinuity, modest changes in velocity and spectral signature between 1700 and 2000 km may reflect impediments to the mantle flow. If such a boundary exists, however, it would be consistent with a boundary of a variable topography with a relief of several hundred kilometers radially. Yet, in visual examination of many cross sections we fail to see evidence for such a discontinuity.

5.6. Hypothesis Testing

The experiments in section 5.4 assume a discontinuity at 670 km, in addition to possible discontinuities near 400, 1000 and 1800 km. To examine the effect of this a priori assumption on the structure away from 670 km, we perform an inversion using a split parameterization with a single discontinuity at 400 km (see Figure 7a). Away from the transition zone, the best fit model from this inversion achieves higher than 93% correlation (Figure 7b, solid line) with S362D400, which contains discontinuous parameterizations at 400 and 670 km. The largest difference between these two models is observed near 670 km; this is expected from the differences in their nominal radial resolution. Near 400 km, the singly split model (at 400 km) shows a correlation of ~90% with S362D400; such a high correlation strongly implies that the a priori assumption of a 670-km dis-

continuity does not significantly affect the resulting velocity structure near 400 km. This model shows nearly perfect correlation with S362C1 (continuous) at depths away from 400 km (Figure 7b, dashed line). The dip in the correlation function at 400 km (dashed line) is less pronounced than that at 670 km (solid line), and its effect is limited to ~200 km radially. Velocity maps at 380 and 420 km (Figures 7c and 7d) show excellent agreement with the corresponding maps of S362D400 (see Plate 6a). The large-scale features of this singly split model in the velocity maps of 650 and 690 km (Figures 7e and 7f) are also consistent with those in the respective maps of the continuous model S362C1 (see Plates 3b and 3c). Because the proposed discontinuity depths at 1000 and 1788 km differ from 670 km by more than 270 km (the difference between the 400- and 670-km discontinuities), we do not expect the multiply split models S362D1000 and S362D1788 to be affected to a greater degree by the a priori presence of the 670-km discontinuity.

Overall, inversions using the three discontinuous radial parameterizations presented in section 5.4 show consistent predictions of 3-D velocity variations away from the proposed discontinuities (at 400, 670, 1000 and 1788 km). There is little evidence for horizontal stratification near 400 and 1000 km. In section 6 we will concentrate on the analysis of the 670-km discontinuity, which has been shown to be a robust boundary, from detailed comparisons of models S362C1 and S362D1.

6. Evaluation of Models

6.1. Variance Reduction

The continuous (S362C1) and the split (S362D1) B spline models achieve significant variance reduction for all data sets used in the inversion. Figure 8 compares the variance reduction of the travel time data set for S362C1 and S362D1. The variance reduction to the travel time measurements is on average ~15% greater for B spline models than for S12 (a continuous model radially parameterized in Chebyshev polynomials). In part, this improvement is expected because of the increase in free model parameters and the fact that S12 was derived using a much smaller data set. S362D1 shows modest improvements over S362C1 in the predictions of ScS and $SS - S$, and predictions to other data sets are comparable to those by S362C1. For the waveform data both models produce similar additional reductions to the data variance relative to those of PREM (Table 2). The small improvement in the vertical component of mantle wave for periods >200 s (8% by both B spline models of this study) is in part related to the extraordinarily high variance reduction of 78% obtained by PREM for this data set. Figure 9 compares sample synthetic seismograms generated using the split model (S362D1) with those of PREM. Clearly, the inclusion of 3-D heterogeneity in the mantle greatly improves the fit to waveforms of both body and mantle wave data.
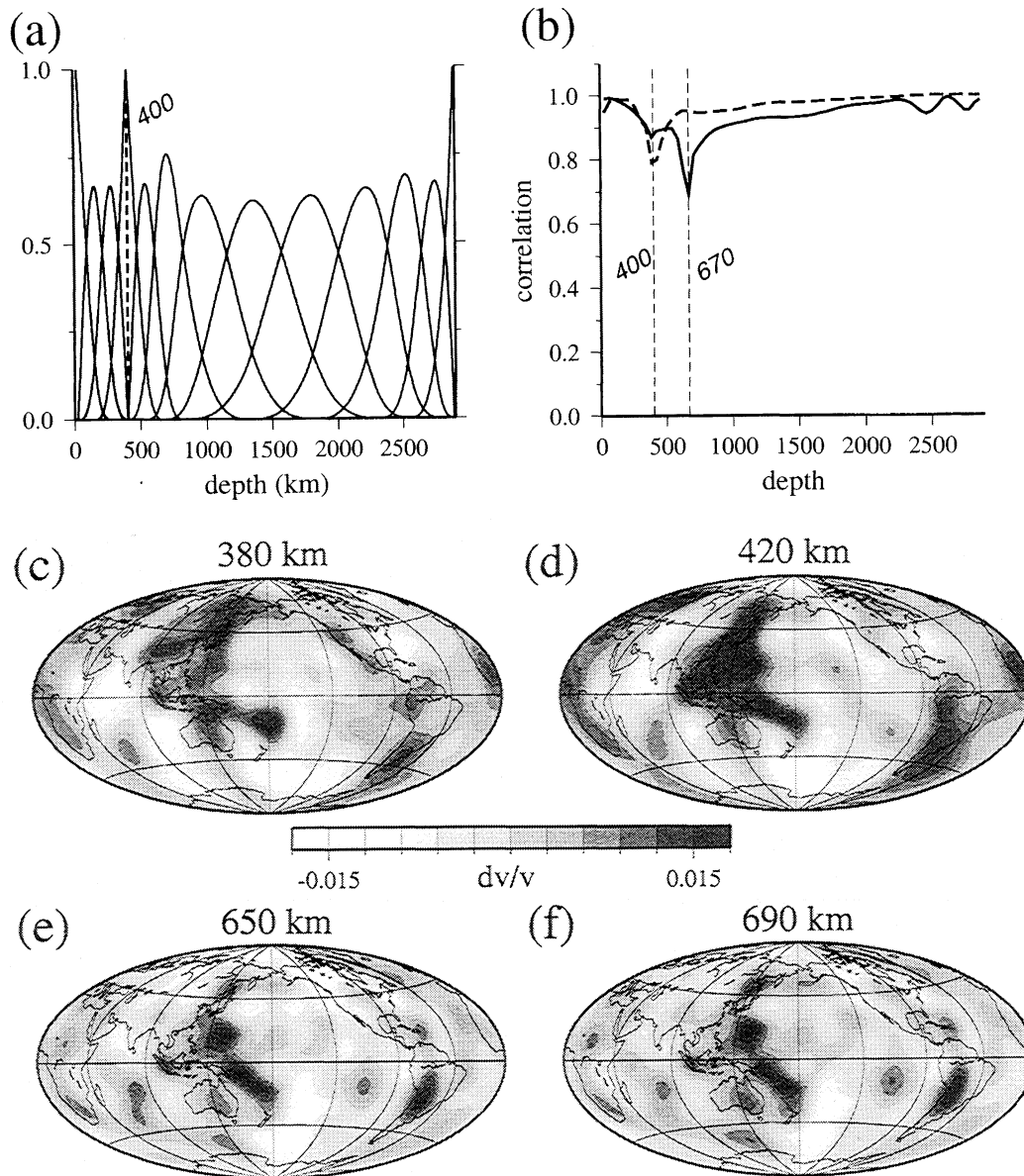
Figure 7. (a) Radial basis function with a discontinuity at 400 km. (b) Solid line, radial correlation between the best fit model (discontinuous at 400 km) and S362D400 (discontinuous at 400 and 670 km); dashed line, radial correlation between this model and the continuous model (see Figure 2a for parameterization). Correlations close to 90% are observed between two discontinuous models, which demonstrates that the assumption of a discontinuity at 670 km does not significantly affect the structure near 400 km. Nearly 80% correlation can be observed between the split model (only at 400 km) and the continuous model, implying relatively small radial variation of velocities near 400 km. (c)–(f) Sample velocity maps for this model at 380, 420, 650, and 690 km, respectively. A very good correlation can be observed between this model and S362D400 (see Plate 6a) at 380 and 420 km. Large-scale features of this model near 670 km are also consistent with those of the continuous model S362C1 (see Plates 3b and 3c).

Overall, split model is as valid as, if not superior to, the continuous model on the basis of variance reduction to the data sets.

6.2. Model Amplitude Analysis

Figure 10a shows the correlation between the continuous and split model at all mantle depths. Including the anomalous depth range of 550 to 770 km (shaded

region), these two models achieve an average correlation of 0.95 or above, shown by the dashed line. Such high correlation demonstrates the robustness of common features in these two models, as well as accuracy of the calculations using the chosen parameterizations. The lowest correlation (∼73%) is observed near 670 km. Figure 10b shows the RMS amplitudes of the heterogeneities of these models. In both models the level of

Travel Time Variance Reduction

○—○ continuous model
□- -□ split model
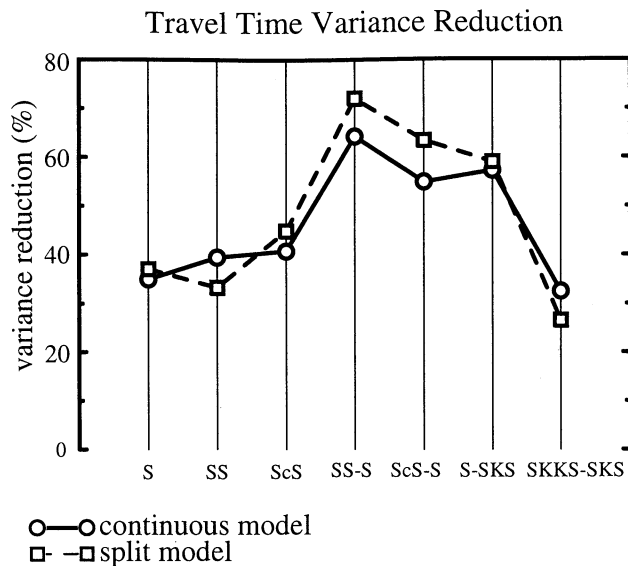
Figure 8. Variance reduction for all travel time measurements. The split model (S362D1) predicts the observed residuals as well as the continuous model (S362C1), if not better.

heterogeneity is ~2.5% in the top 100 km, and the amplitude decays nearly linearly in the next 300 km. A steep falloff in RMS amplitude (to <0.4%) is observed in the split model immediately below the 670-km discontinuity, and the low amplitude continues down to ~1800 km. A significant reduction in the RMS amplitude is also present in the continuous model, although the transition takes place over a wider depth range (see shaded region). This feature provides additional evidence for distinct thermal/chemical processes in the upper and lower mantle. A gradual increase in the level of heterogeneity at depths below 1800 km is also observed in both models.

6.3. Mantle Cross Sections

Cross sections of S362C1 (continuous) and S362D1 (split) show excellent agreement in the main patterns of lateral heterogeneities, despite the different choices of radial basis functions. Both models display significant lateral and radial variations from the transition zone to the lower mantle, which reflect the complexity in the pattern of mantle convection across the 670-km discontinuity. For brevity, we will show four sample velocity profiles of the split model S362D1 for all mantle depths.

Plate 9a shows a polar cross section through North America and Eurasia. In the top 200 km the velocities are well correlated with the continent–ocean signature, with intense velocity highs underlying these two continents, and lower velocities beneath the eastern Pacific and Indian Oceans. The effect of the continental roots is diminished in the transition zone, as the large-scale high-velocity anomalies change sign near 400 km (shown by the outermost white circle); on the other hand, slow

velocities under the oceans are fairly continuous at this depth. In the lower mantle, long-wavelength fast velocities, from the southern Indian ocean to northwest China, span thousands of kilometers laterally and extend down to the CMB radially. Fast velocity anomalies underlie the southeast Pacific and extend farther south toward the CMB. Negative perturbations, with absolute amplitudes exceeding 2.5%, are observed at the CMB in the eastern Pacific.

Plate 9b presents a cross section through Africa and Eurasia. An important feature is a low-velocity anomaly under Africa which extends vertically from the base of the mantle to the 670-km discontinuity and appears to shift to the northeast at shallower depths. This result is in good agreement with the velocity profiles shown by *Ritsema et al.* [1999] and *Mégnin and Romanowicz* [2001], although controversy still remains whether the slow domain actually continues into the upper mantle. Whatever the case is, the observed lateral shift of the slow anomalies in the upper mantle would suggest some interference from the 670-km boundary. Another instance of potential impedance at 670 km is a sharp change of velocity gradients beneath Eurasia, where a slow domain is sandwiched by the cold continental root in the top 400 km and a high-velocity domain in the lower mantle. The subduction signature under Japan does not appear to extend beyond the 670-km boundary.

A slice through the central Pacific and South America (Plate 9c) features lower mantle ultra low-velocity perturbations corresponding to the equatorial Pacific plume group [*Dziewonski et al.*, 1991, 1993], which extend upward for over 1000 km. The absolute amplitude of these anomalies exceeds 3% at the base of the mantle and attenuates with decreasing depth. These anomalies are generally overlain by near average, or faster than average, velocities at mid-mantle depths or near the 670-km boundary, which appear to impede vertical upwelling. Fast velocities under South America, which are

Table 2. Variance Reduction for Waveforms

Data Type	Variance Reduction, %	
	Continuous	Split
Body waves set 1 ($T > 45$ s, V)	34	34
Body waves set 1 ($T > 45$ s, T)	25	26
Body waves set 2 ($T > 45$ s, V)	35	37
Body waves set 2 (T > 45 s, T)	32	32
Mantle waves ($T > 85$ s, V)	48	48
Mantle waves ($T > 85$ s, T)	80	81
Mantle waves ($T > 135$ s, V)	46	47
Mantle waves ($T > 135$ s, T)	38	39
Mantle waves ($T > 200$ s, V)	8	8
Mantle waves ($T > 200$ s, T)	35	35

Set 1 represents a data set with recordings from 1991–1998; set 2 represents a data set with recordings from 1977–1990; T, period; V, vertical; T, transverse.
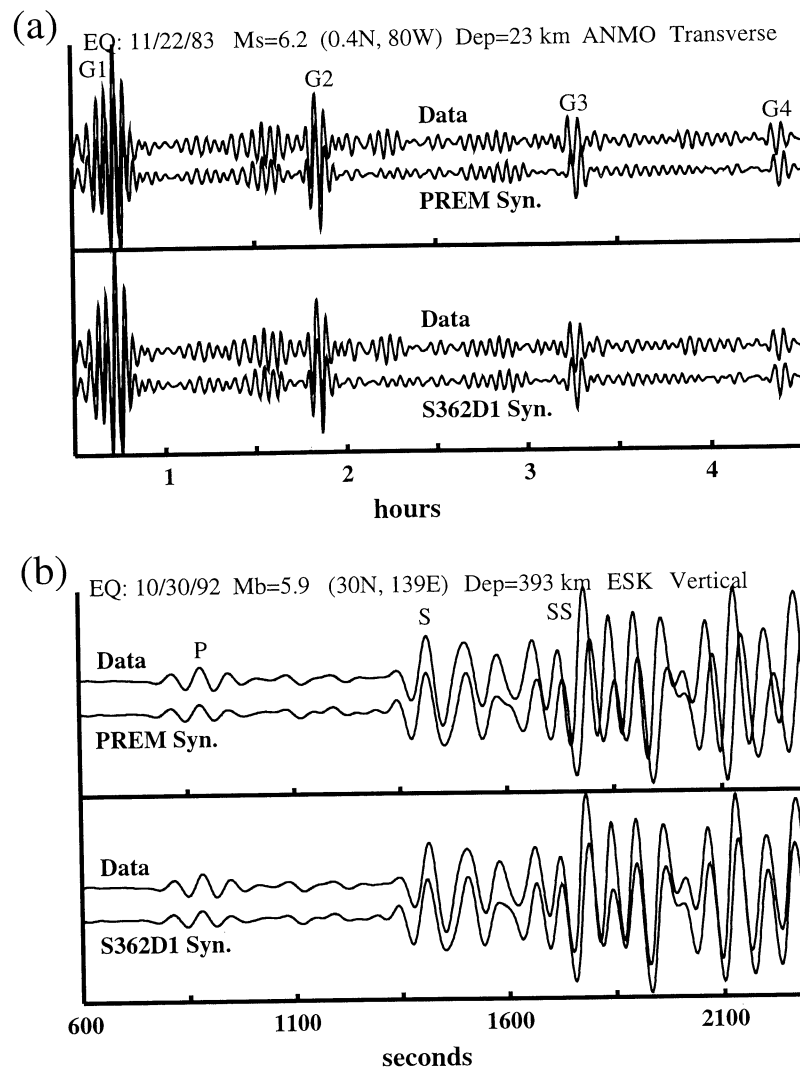
Figure 9.	(a) Transverse component of a surface wave recording of an earthquake near the coast of Equador on November 23, 1983, from station ANMO. (b) Vertical component of a body wave recording of an earthquake to the south of Honshu by station ESK. Synthetic seismograms using model S362D1 better predict phase and amplitude of both surface and body wave phases, in relation to using PREM.

likely to be associated with the subduction of the Nazca plate, continue at least down to 1500 km while maintaining the dip angle of the Benioff Zone. Although this is consistent with a recent shear velocity study by *Mégnin and Romanowicz* [2001], which may suggest slab penetration at the 670-km boundary in this region, the lateral extent of the anomaly appears to be limited in our model (see Plate 3). There are features, e.g., fast velocity "columns" to the west of the South American slab signature, which cannot be associated with any known geological events. Their existence demonstrates the complexity of the Earth's mantle and the limitation of our current understanding of its processes. Fast velocities beneath Africa and Eurasia appear to extend into the transition zone.

A cross section through Australia and northern India (Plate 9d) displays alternating signatures resulting from the locations of continents and oceans in the upper mantle: fast velocities exist in Australia, South America, and Eurasia, and slow velocities exist in the Atlantic and the western and central Pacific. In the lower mantle, fast velocity anomalies extend from Indonesia to the Mediterranean nearly horizontally for more than 5000 km (the Tethys Trough [*Woodhouse and Dziewonski*, 1989; *Dziewonski et al.*, 1991, 1993]). Also present are fast velocities that could be related to subduction under New Zealand which continue down to at least 1800-km depth. No breakage in the radial velocity variations is visible close to 1000 and 1800 km.

In general, the cross sections of S362D1 illustrate that not all subducted slabs penetrate into the lower mantle, nor do all plumes propagate into the upper mantle without being partially blocked or deflected. Regarding the behavior of slabs near the 670-km boundary, seismic imaging of subduction zones has produced diverse results [*Zhou and Clayton*, 1990; *van der Hilst et al.*,

(a)

(b)
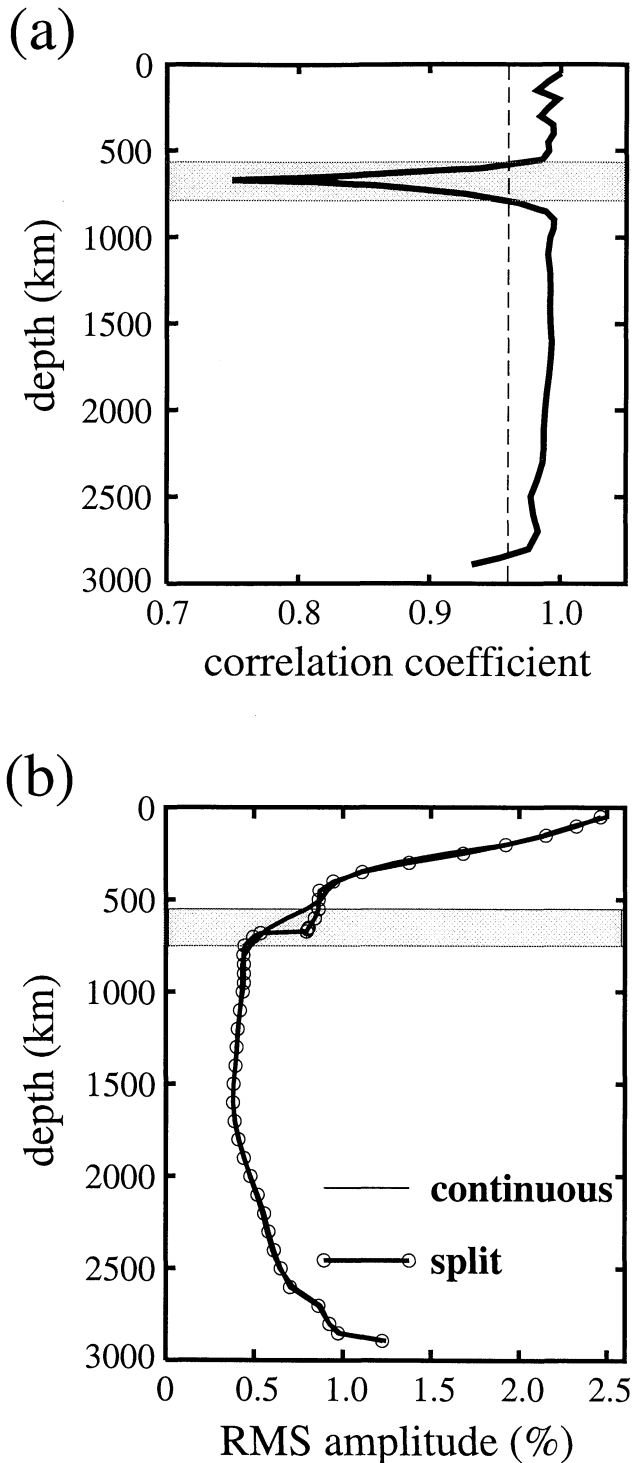
Figure 10. (a) Radial correlation between S362C1 and S362D1. The dashed line denotes the average correlation throughout the mantle. The shaded region, between 540 and 770 km, highlights depths with lower than average correlation. (b) Root-mean-square amplitudes of mantle heterogeneities. A sharp falloff of heterogeneities is predicted by the split model. The shaded region marks the region of the largest difference between these two models.

1991; *Fukao et al.*, 1992]. Our results are consistent with a model of partial stratification which can significantly affect local-scale convection. In some areas, e.g., the western Pacific, the lower mantle layer may be per-

meable to events of substantial mass and heat perturbations, though the lateral extent and amplitudes of the anomalies vary significantly. Changes in mineral elastic properties and chemical variations may also affect the velocities near the 670-km discontinuity. *Ringwood* [1994] suggests that the combined effect of (1) differentiation of oceanic lithosphere into basaltic and depleted peridotitic layers and (2) delamination and transformation of former oceanic crust to a "garnetite" layer can effectively hinder whole mantle convection at some locations. Some anomalies in the lower mantle, such as the long-wavelength fast velocities in the eastern Pacific (Plates 9a, 9c, and 9d), provide further evidence for the characteristic differences between the upper and lower mantle that are not well understood at the present time.

Cross sections of the continuous model (not shown here) also display significant changes in the amplitude and sign of large-scale heterogeneities near 670 km, although these changes take place over a depth range of 100–200 km. Both the continuous and split models appear to favor a possible change of flow, on the global scale, near 670 km. Some large-scale velocity structures, e.g., beneath Africa and Indonesia in Plate 9, also appear to be somewhat discontinuous across the 400-km discontinuity. However, the distribution is limited to regional scale, and the transition is much more gradual than that of the boundary between the upper and lower mantle. No detectable horizontal stratification is present at depths close to 1000 and 1800 km (denoted by the two inner white circles), as fast velocities under India and South America and slow velocities under Africa and the central Pacific all continue across these depths without significant changes in shape or amplitude.

7. Discussion

The principal result of this study is illustrated by Plates 3e to 3h: There is little correlation between the heterogeneities above the 670-km discontinuity and those below it. There are regions of fast transition-zone velocity that lie on top of regions of predominantly slower than average velocity in the lower mantle, e.g., the long-wavelength structure under South America-Atlantic-western Africa. On the other hand, there are low-velocity structures in the transition zone that are underlain by higher than average velocities in the lower mantle. A striking example is the area extending from the Caribbean to the eastern Pacific. The only locations that strongly support a continuous slab transport across the boundary is a region from the Philippine Sea to Tonga and a small area under Peru.

To the extent that this snapshot picture can be considered representative of the flux, either thermal or compositional, across the boundary, it seems that the area across which flow occurs is limited. Thus our results support at least a partial separation of the flow. It does not mean that there is no exchange of material between the upper and lower mantle, but the implication is that this flow is significantly impeded.

S362D1

(a)   (b)

(c)   (d)

-1.5   dv/v (%)   1.5
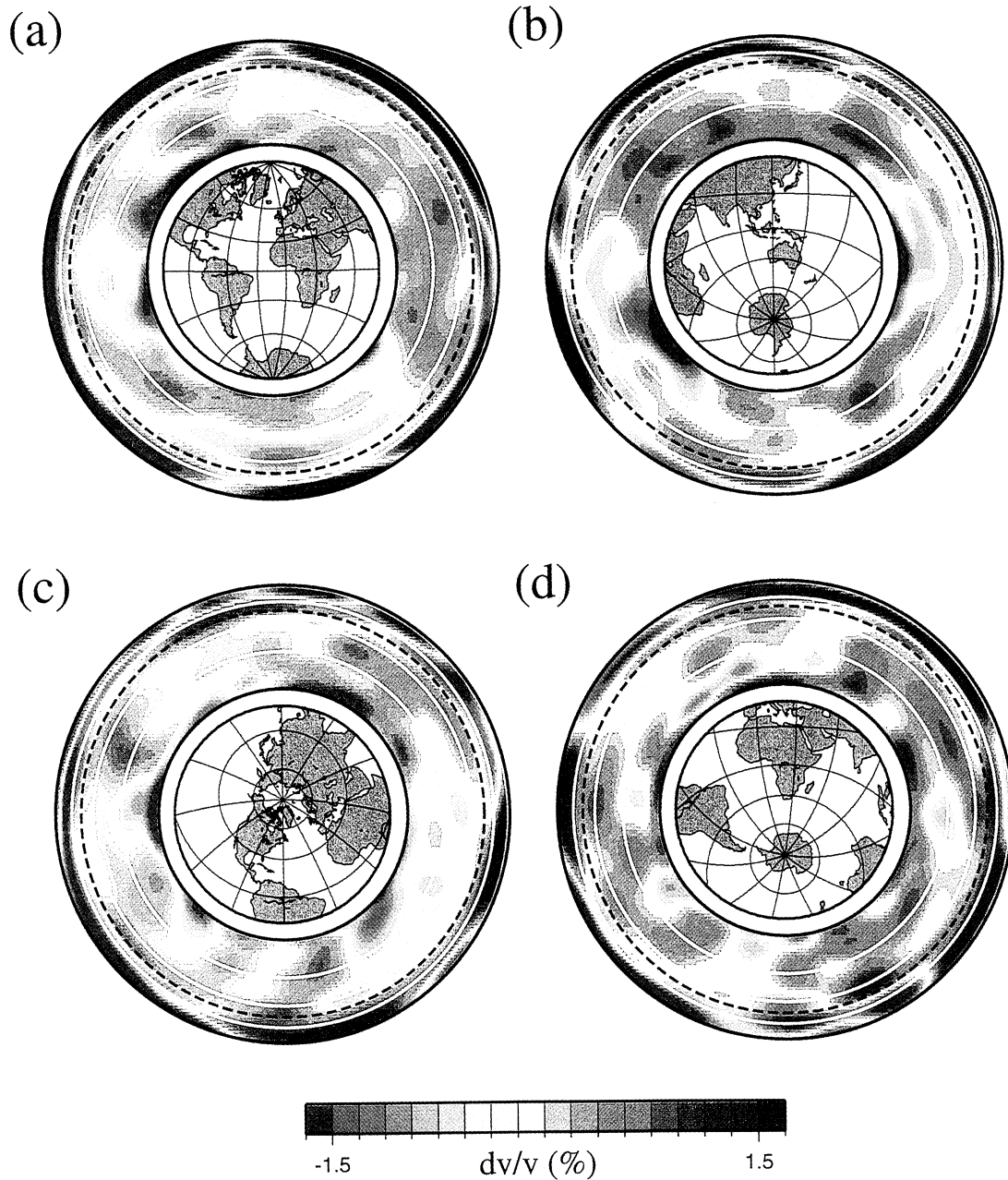
Plate 9. Cross sections of S362D1 (split) through four different angles. The thick circle inside the inset map indicates the great circle defining the cross section. The outermost solid circle is the Moho surface, the second is the 670-km discontinuity, and the innermost one corresponds to the CMB. The three white circles (starting from the outermost) mark the depths of 400, 1000, and 1800 km, respectively. (a) A cross section through Europe with a pole location of (0°N, 15°W). (b) A cross section through Africa and Eurasia; pole location is (37°S, 120°E). (c) A cross section through South America; pole location is (75°N, 60°W). (d) A cross section through Australia and India; pole location is (45°S, 20°W).

There is a wide body of evidence that supports the idea of a major change near the 670-km depth in the path of the subducted material. A subset of such evidence includes (1) cessation of seismicity, (2) bending or breaking of slabs in several subduction zones, suggested by deep earthquakes 200–300 km outside of clearly defined Benioff zones [*Isacks and Molnar*, 1971; *Ekström et al.*, 1990], (3) possible folding of slabs in some subduction zones [*Giardini and Woodhouse*, 1984], (4) geochemical evidence for subducted material in the transition zone [*Collerson et al.*, 2000], and (5) increasing width of the positive velocity anomalies in major subduction zones near the base of the upper mantle [*Woodhouse and Dziewonski*, 1984].

In addition, studies of the topography of the 670-km discontinuity [e.g., *Shearer and Masters*, 1992; *Flanagan and Shearer*, 1998; *Gu et al.*, 1998] show strong depression of lateral scales of 2000–3000 km near major subduction zones such as the western Pacific; this implies possible ponding (as well as horizontal flattening) of cold slab material near these subduction zones.

8. Other Issues

For the last several years the results from "high-resolution tomography" have been interpreted as documenting slab penetration [*Vidale*, 1994; *van der Hilst et al.*, 1997] into the lower mantle and their coherent transport to the CMB. Some of the current literature considers it as an established fact [e.g., *McNutt*, 1999]. One of the frequently cited examples is that of the "Farallon slab".

In Plate 10 we compare cross sections through six *S* velocity models of the mantle. This comparison has a dual purpose. One is to examine the images of the Farallon slab, and the other is to assess the common presence of very large, slow anomalies that extend from the CMB to mid-mantle depths and may, on occasion, reach the 670-km discontinuity or above.

The current study is represented by Plate 10a. Model S20A (Plate 10b, [*Ekström and Dziewonski*, 1998]) was obtained from a similar data collection as the one used here, but a global parameterization in terms of spherical harmonics and Chebyshev polynomials; the similarity between the two models implies that the results are not strongly dependent on the type of the basis functions. Plate 10c is the 4 degree block model of *Masters et al.* [1999], obtained from travel times, surface wave dispersion, and splitting of normal modes. Plate 10d is a degree 24 model of *Mégnin and Romanowicz* [2001], obtained from Love wave dispersion and inversion of body waveforms using nonlinear coupling theory [*Li and Romanowicz*, 1995]. Plate 10e shows the degree 20 model of *Ritsema et al.* [1999], obtained through inversion of travel times, dispersion of surface waves (including overtones) and splitting of normal modes. Finally, plate 10f shows the model of *Grand et al.* [1997] obtained

through inversion of shear wave travel times (including *ScS* and multiple *S*, as well as differential travel times). The models in Plate 10a, 10c and 10f are parameterized using local basis functions, whereas the models in 10b, 10d and 10e use global basis functions. It is difficult to detect any consistent differences between these two groups of models due to parameterization.

The model by *Grand et al.* [1997] is notably different from the other five in terms of the amplitude of the anomalies. While its amplitudes near the surface and CMB are comparable with those of other models, they are significantly lower from ∼300 km to 2600 km. This model shows very little structure in the transition zone and, with some exceptions, also in the middle mantle. In addition to a distinct Farallon plate high-velocity anomaly (down to the CMB), there are other positive anomalies near the bottom of the mantle, e.g., two weaker anomalies spanning the lower mantle on either side of the Farallon plate. These, on their own, could be easily dismissed as being at nearly the noise level. However, if we look at the other five models, we can see that the same, or nearly the same, structure shows up in all the models. It would therefore seem the proper interpretation of the Farallon plate image is not that we have caught a slab along its journey toward the graveyard at the CMB, but that there exists a wide (2000–3000 km) high-velocity structure in the lower mantle which is not related in a clear way to upper mantle tectonics.

The study of *van der Voo et al.* [1999] associated a double slab under Asia, present in the *P* velocity model of *Bijwaard et al.* [1998], as evidence for a fossil slab ∼200 Myr old. A corresponding cross section through that region (Plate 11) for the six *S* velocity models of Plate 10 exhibit complexity similar to that of the Farallon slab. In most models there appears to be a significant horizontal deflection of the downgoing slab in the transition zone, particularly in model SAW24B16. The structure below 1300 km is clearly dominated by a high-velocity pattern that consists of three nearly equally-spaced anomalies. The high-velocity regime spans ∼3000 km laterally in the bottom 800 km of the lower mantle. The suggestion of a double slab is not sufficient to describe the complexity of this structure. Considering the "multiple slab" in Plate 10, there is no reason to assume that a similar effect could not be present under Asia, i.e., the observed anomalies are simply parts of the circum-Pacific ring of fast velocities [*Dziewonski*, 1984]. In addition, some geodynamic modeling results, e.g., *Ricard et al.* [1993], predict that a 200 Myr old slab should have been already at the CMB, rather than extend into the upper mantle as in *Bijwaard et al.*'s [1998] model. It is likely that the prevailing interpretations of the tomographic images as representing whole mantle convection, e.g. as assumed in the review paper by *Tackley* [2000], are over-simplified and that we still do not have a good understanding of the circulation of
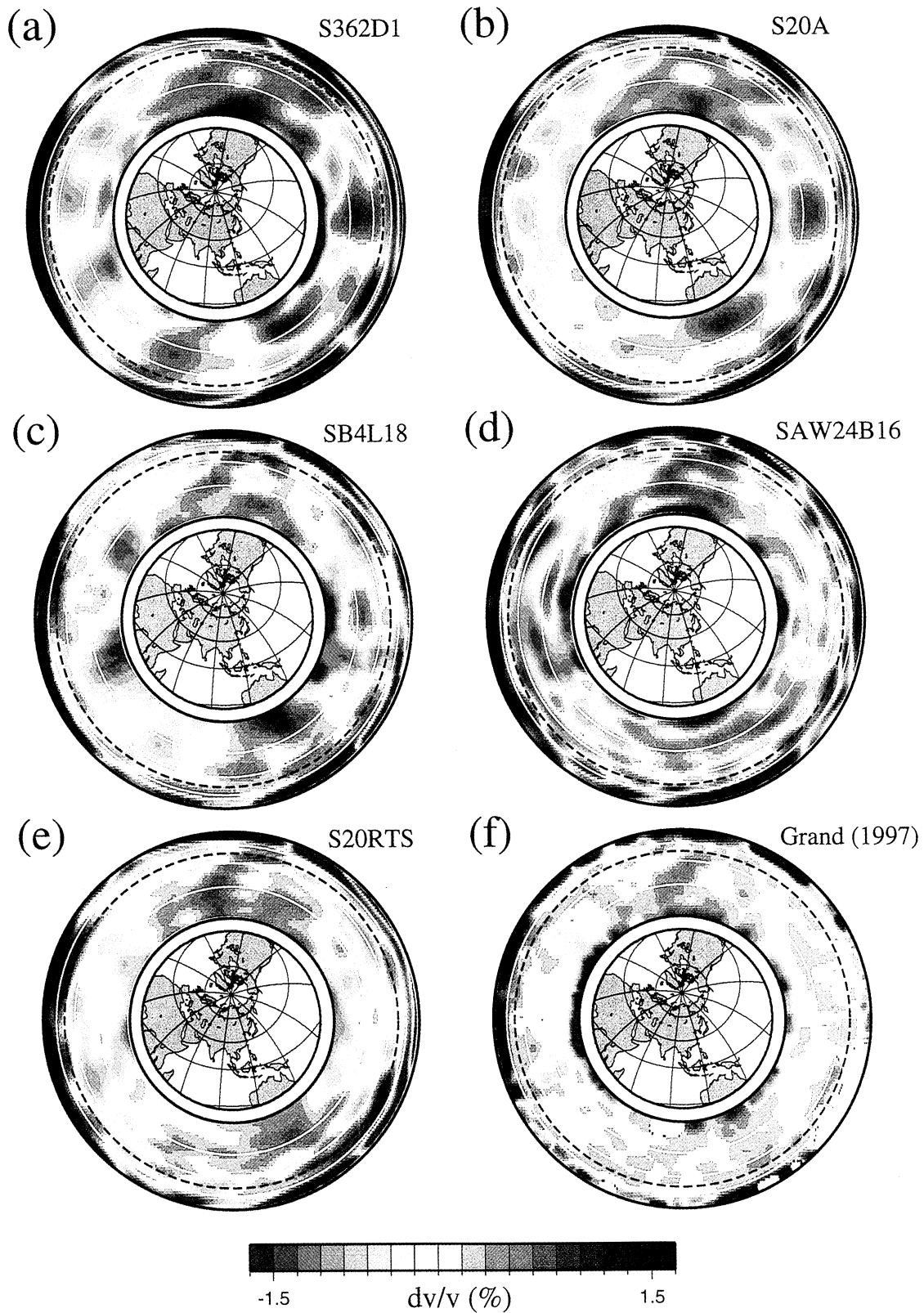
Plate 10. Cross sections with a pole location of (58°N, 100°E) for six models (see Plate 9 for definition of colors and symbols). The models are: (a) S362D1 of this study, (b) S20A [*Ekström and Dziewonski*, 1998], (c) SB4L18 of *Masters et al.* [1999], (d) SAW24B16 of *Mégnin and Romanowicz* [2001], (e) S20RTS of *Ritsema et al.* [1999], and (f) model of *Grand et al.* [1997]. The complex velocity pattern under North America and the eastern Pacific cannot be fully accounted for by simple subduction of the Farallon slab.
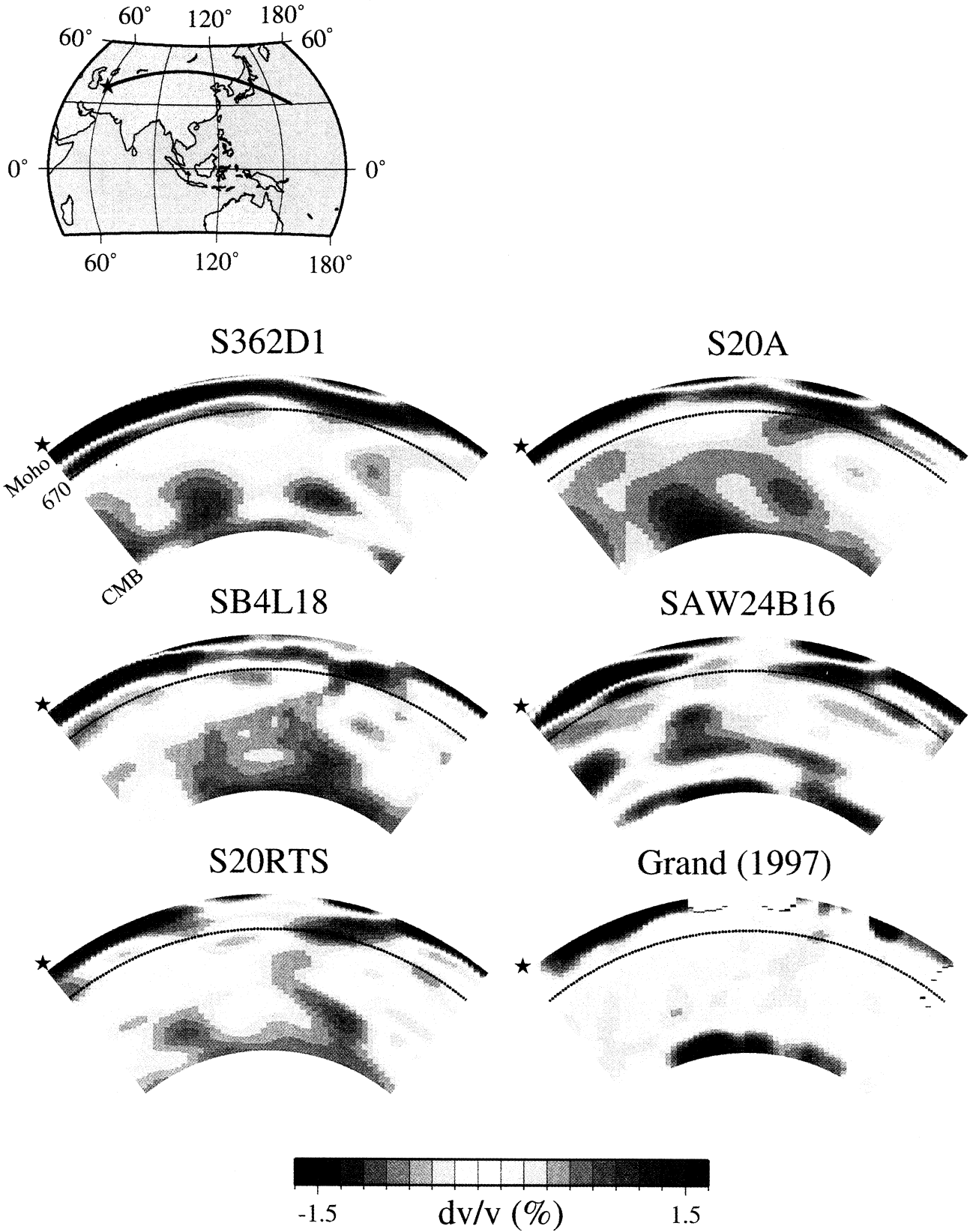
Plate 11. Regional cross sections with a pole location of (43.5°N, 77.8°W) for the same models as in Plate 10. In the top left panel, the red line shows the location of the cross section along the minor arc path. Red stars denote the beginning of each cross section. The complexity of the velocity structure is comparable to that in Plate 10, and need not be associated with a fossil Jurassic slab.

the material in the mantle, as well as the relationship between a snapshot of the mantle and its dynamics.

In addition to high velocity anomalies, we also have to explain the megaplumes, such as the African plume or the equatorial Pacific plume group. While the avalanche model of *Tackley et al.* [1993, 1994] predicts some of the effects associated with the 670-km and CMB boundaries, its high-temperature (low-velocity) anomalies are not similar to those obtained in the tomographic models. In those studies, as well as in other convection models, high temperature features tend to be rather narrow. The megaplumes are about as wide as they are tall. The amplitude of the anomaly is the largest near the CMB but decreases slowly over some 2000-km height.

Kellogg et al. [1999] proposed that megaplumes represent a deformed surface of an abyssal layer composed of primordial mantle material. This layer has different composition than the well-mixed remaining part of the mantle. The abyssal layer is intrinsically denser, but because of its higher temperature the density contrast is greatly diminished. Laboratory experiments along similar lines have been described by *Davaille* [1999]. In a way, the model is appealing because it could explain the large-wavelength structure obtained in the tomographic models as well as shallower origin of hotspots than the CMB. However, experiments by *Davaille* [1999] required that the abyssal layer be more viscous by 2 orders of magnitude, which would be difficult to obtain if it were also hotter, since viscosity decreases with temperature. Our experiments with introduction of discontinuities in the lower mantle (near 1000 and 1800 km) and examination of cross sections do not reveal the clear presence of additional discontinuities, even if they were to have a significant topography.

It appears that the images derived from seismic tomography do not have a clear physical explanation as yet. While the increased resolution is highly desirable, for the results to be meaningful it should not be limited to a particular class of structures, such as subduction zones. The slab-centric approach could lead to distorted perceptions of the dynamics of the Earth.

While our modeling approach has provided new ways to image the Earth's interior, it is equally important to explore the limitations of our analysis. There may be artifacts associated with the uncertainties in the measurements, insufficient data coverage in parts of the mantle and, possibly, model parameterizations. These factors, however, do not affect the main conclusion of this study, which is that the long-wavelength velocity structure and power spectra in the transition zone are significantly different from those at depths below 750 km. This is supported by models with and without a discontinuous radial parameterization across the 670-km boundary in depth ranges resolvable with the available data; this robust feature suggests at least a partial separation in the flow pattern between the upper and lower mantle. Furthermore, our data sets do not require a significant flow change near 400, 1000, and 1800 km, though a gradual

increase in the power of the low-degree harmonics is observed in the depth range of 1800–2000 km. Future consideration and modeling of the effects associated with anisotropy and boundary topography of transition zone discontinuities can improve our overall understanding of mantle shear velocity structure.

Appendix A: Damping Matrix

The inverse problem for our system of equations is underdetermined, and we choose to stablize the inversion by imposing horizontal and radial damping to the $(\mathbf{A}^T \cdot \mathbf{A})$ matrix. The system of equations can be written as

$$(\mathbf{A}^T \cdot \mathbf{A} + \mathbf{D}) \cdot \mathbf{x} = \mathbf{A}^T \cdot \mathbf{d}. \tag{A1}$$

$\mathbf{D}$ is a symmetric 3-D damping matrix which depends on a horizontal damping matrix $\mathbf{D}_h$ and radial damping matrix $\mathbf{D}_r$,

$$\mathbf{D} = \gamma_h \mathbf{D}_h \cdot \mathbf{I} + \gamma_r \mathbf{D}_r; \tag{A2}$$

γ_h and γ_r are empirically determined weights. The horizontal damping matrix $\mathbf{D}_h$ only contributes to the near diagonal elements of the inner product matrix $(\mathbf{A}^T \cdot \mathbf{A})$.

We can express the value of $\delta v / v_0$ at a given point in the Earth as

$$\Phi = \sum_{ij} C_{ij} S_j(\Delta) B_i(r), \tag{A3}$$

where $S_j(\Delta)$ is the jth horizontal B spline, which is a function of the arc distance Δ away from the given point. C_{ij} is the unknown coefficient and B_i is the ith radial spline. To partition the effect of horizontal and radial damping, we define the following gradients:

$$\nabla_1 \Phi = \frac{\partial \Phi}{\partial \theta} \hat{\mathbf{e}}_\theta + \frac{1}{\sin(\theta)} \frac{\partial \Phi}{\partial \phi} \hat{\mathbf{e}}_\phi, \quad \nabla_2 \Phi = \frac{\partial \Phi}{\partial r} \hat{\mathbf{e}}_r. \tag{A4}$$

To obtain the radial damping matrix $\mathbf{D}_r$, we require (similar to *Liu and Dziewonski* [1998]),

$$\int_{r_0}^{r_1} \|\nabla_2 \Phi\|^2 dr = \int_{r_0}^{r_1} \| \sum_{i,j} C_{ij} S_j(\theta, \phi) \frac{dB_i(r - r_i)}{dr} \|^2 dr$$

$$= \min, \tag{A5}$$

where r_0 and r_1 range between r_{CMB} and r_{Moho} and $r_0 > r_1$. The mnth element of the radial damping matrix $\mathbf{D}_r$ is computed by

$$(D_r)_{mn} = \int_{r_0}^{r_1} \frac{dB_m(r - r_m)}{dr} \frac{dB_n(r - r_n)}{dr} dr. \tag{A6}$$

The first derivatives dB_m/dr and dB_n/dr are given by *Liu* [1997]. An element of the matrix is zero when mth and nth splines do not overlap.

To obtain the horizontal damping matrix $\mathbf{D}_h$, we require that

$$\int_\Omega \|\nabla_1 \Phi\|^2 d\Omega = \int_\Omega \left(\frac{\partial \Phi}{\partial \theta} \right)^2 + \left(\frac{1}{\sin(\theta)} \frac{\partial \Phi}{\partial \phi} \right)^2 d\Omega = \min,$$

where Ω is a two-dimensional surface. To simplify notations we will replace the unknown coefficient C_{ij} in (A3) by C_i and evaluate the horizontal damping matrix $\mathbf{D}_h$ independently. By setting the first derivatives of the integral with respect to model coefficients $C_{i'}$ to zero, we can obtain

$$\frac{\partial}{\partial C_{i'}} \int_\Omega \left(\frac{\partial \Phi}{\partial \theta}\right)^2 d\Omega = 2 \int_\theta \int_\phi \left(\sum_i C_i \frac{\partial S(\Delta_i)}{\partial \Delta_i} \frac{\partial \Delta_i}{\partial \theta}\right)$$

$$\cdot \frac{\partial S(\Delta_{i'})}{\partial \Delta_{i'}} \frac{\partial \Delta_{i'}}{\partial \theta} \sin(\theta) d\theta d\phi, \qquad (A8)$$

$$\frac{\partial}{\partial C_{i'}} \int_\Omega \left(\frac{1}{\sin(\theta)}\frac{\partial \Phi}{\partial \phi}\right)^2 d\Omega = 2 \int_\theta \int_\phi \frac{1}{\sin(\theta)} \left(\sum_i C_i\right.$$

$$\left.\cdot \frac{\partial S(\Delta_i)}{\partial \Delta_i}\right) \frac{\partial \Delta_i}{\partial \Delta_{i'}} \frac{\partial S(\Delta_{i'})}{\partial \phi} \frac{\partial \Delta_{i'}}{\partial \phi} d\theta d\phi. \qquad (A9)$$

The sum of these two terms renders the damping coefficients for the ith spline due to interaction with the i'th spline. Simple trigonometry gives

$$\cos(\Delta) = \cos(\theta_s)\cos(\theta) + \sin(\theta_s)\sin(\theta)\cos(\phi - \phi_s), \qquad (A10)$$

where θ_s and ϕ_s are coordinates of any given point on the spherical surface. Partial derivative of Δ with respect to θ becomes

$$\frac{\partial \Delta}{\partial \theta} = \frac{1}{\sin(\Delta)}\left[\cos(\theta_s)\sin(\theta) - \sin(\theta_s)\cos(\theta)\cos(\phi - \phi_s)\right] \qquad (A11)$$

and partial derivative of Δ with respect to ϕ becomes

$$\frac{\partial \Delta}{\partial \phi} = \frac{1}{\sin(\Delta)}\left[\sin(\theta_s)\sin(\theta)\sin(\phi - \phi_s)\right]. \qquad (A12)$$

Furthermore, since the first derivative of $S(\Delta)$ can be derived from differentiating expression (2),

$$S'(\Delta) = \begin{cases} \frac{9}{4h}\left(\frac{\Delta}{h}\right)^2 - \frac{3}{h}\left(\frac{\Delta}{h}\right) & \Delta \leq h \\ \frac{3}{4h}\left(2 - \frac{\Delta}{h}\right)^2, & h \leq \Delta \leq 2h \\ 0, & \Delta > 2h, \end{cases} \qquad (A13)$$

where h is the average distance between two knots, then partial derivatives of $S(\Delta)$ with respect to θ and ϕ can be evaluated from the chain rule $\partial S(\Delta)/\partial \theta = S'(\Delta)(\partial \Delta/\partial \theta)$, and $\partial S(\Delta)/\partial \phi = S'(\Delta)(\partial \Delta/\partial \phi)$. Finally, substitute $\partial S(\Delta)/\partial \theta$ and $\partial S(\Delta)/\partial \phi$ into (A8) and (A9), we can effectively compute the coefficients for the damping matrix $\mathbf{D}_h$ by performing numerical integrations over all the θ and ϕ values. It turns out that most of the damping coefficients are zero since only splines that fall within twice the average distance between two spline nodes have nonzero effects on the current spline.

References

Bijwaard, H., W. Spakman, and R. E. Engdahl, Closing the gap between regional and global travel time tomography, *J. Geophys. Res.*, *103*, 30,055-30,078, 1998.

Bunge, H. P., R. M. Richards, and J. R. Baumgardner, Effect of depth-dependent viscosity on the planform of mantle convection, *Nature*, *379*, 436-438, 1996.

Collerson, K. D., S. Hapugoda, B. S. Kamber, and Q. Williams, Rocks from the mantle transition zone: Majorite bearing xenoliths from Malaita, southwest Pacific, *Science*, *288*, 1215-1223, 2000.

Davaille, A., Simultaneous generation of hotspots and superswells by convection in a heterogeneous planetary mantle, *Nature*, *402*, 756-760, 1999.

de Boor, C., *A Practical Guide to Splines*, Springer-Verlag, New York, 1978.

Durek, J. J., G. Ekström, and S. Tsuboi, Effect of anelastic heterogeneity on measurements of fundamental mode attenuation, *Eos Trans. AGU*, *74*(43), Fall Meet. Suppl., 439, 1993.

Dziewonski, A. M., Mapping the lower mantle: Determination of lateral heterogeneity in P velocity up to degree and order 6, *J. Geophys. Res.*, *89*, 5929-5952, 1984.

Dziewonski, A. M., and D. L. Anderson, Preliminary reference Earth model, *Phys. Earth Planet. Inter.*, *25*, 297-356, 1981.

Dziewonski, A. M., and W.-J. Su, Negative velocity anomalies from mid-ocean ridges to CMB, *Eos Trans. AGU*, *74*(43), Fall Meet. Suppl., 76, 1993.

Dziewonski, A. M., W.-J. Su, and R. L. Woodward, Grand structures of the Earth's Interior, *Eos Trans. AGU*, *72*(44), Fall Meet. Suppl., 451, 1991.

Dziewonski, A. M., A. M. Forte, W.-J. Su, and R. L. Woodward, Seismic tomography and geodynamics, in *Relating Geophysical Structures and Process: The Jeffreys Volume*, *Geophys. Monogr. Ser.*, vol.76, edited by K. Aki and R. Dmowska, pp.67-105, AGU, Washington, D.C., 1993.

Ekström, G., and A. M. Dziewonski, The unique anisotropy of the Pacific upper mantle, *Nature*, *394*, 168-172, 1998.

Ekström, G., A. M. Dziewonski, and J. Ibanez, Deep earthquakes outside slabs, *Eos Trans. AGU*, *71*(43), 1462, 1990.

Ekström, G., J. Tromp, and E. W. F. Larson, Measurements and global models of surface wave propagation, *J. Geophys. Res.*, *102*, 8137-8157, 1997.

Flanagan, M. P., and P. M. Shearer, Global mapping of topography on transition zone velocity discontinuities by stacking SS precursors, *J. Geophys. Res.*, *103*, 2673-2692, 1998.

Forte, A. M., and R. L. Woodward, Joint seismic and geodynamic constraints on large-scale vertical flow across the 670 km seismic discontinuity, paper presented at Fourth SEDI Symposium, Can. Geophys. Union, Whistler Mountain, BC, Canada, Aug., 1994.

Forte, A. M., and R. L. Woodward, Seismic-geodynamic constraints on three-dimensional structure, vertical flow, and heat transfer in the mantle, *J. Geophys. Res.*, *102*, 17,981-17,994, 1997.

Forte, A. M., A. M. Dziewonski, and R. L. Woodward, Aspherical structure of the mantle, tectonic plate motions,

nonhydrostatic geoid and topography of the core-mantle boundary, in *Dynamics of the Earth's Deep Interior and Earth Rotation, Geophys. Monogr. Ser.*, vol.72, edited by J.-L Le Mouël, pp.135-166, AGU, Washington, D.C., 1993.

Fukao, Y., M. Obayashi, H. Inoue, and M. Nenbai, Subducting slabs stagnant in the mantle transition zone, *J. Geophys. Res., 97*, 4809-4822, 1992.

Giardini, D., and J. H. Woodhouse, Deep seismicity and modes of deformation in Tonga subduction zone, *Nature, 307*, 505-509, 1984.

Gossler, J., and R. Kind, Seismic evidence for very deep roots of continents, *Earth Planet. Sci. Lett., 138*, 1-13, 1996.

Grand, S. P., R. D. van der Hilst, and S. Widiyantoro, Global seismic tomography: a snapshot of convection in the Earth, *GSA Today, 7*, 1-7, 1997.

Gu, Y., A. M. Dziewonski, and C. B. Agee, Global decorrelation of the topography of transition zone discontinuities, *Earth Planet. Sci. Lett., 157*, 57-67, 1998.

Gu, Y., A. M. Dziewonski, and G. Ekström, Radial anisotropy of the upper mantle from waveform and travel time inversions, *Eos Trans. AGU, 80*(17), Spring Meet. Suppl., S221, 1999.

Ho-Liu, P. H. Y., J.-P, Montagner, and H. Kanamori, Comparison of iterative back-projection inversion and generalized inversion without blocks; case studies in attenuation tomography, *Geophys. J. R. Astron. Soc., 97*, 19-29, 1989.

Isacks, B., and P. Molnar, Distribution of stresses in the descending lithosphere from a global survey of focal mechanism solutions of mantle earthquakes, *Rev. Geophys., 9*, 103-174, 1971.

Jordan, T. H., P. Puster, G. A. Glatzmaier, and P. J. Tackley, Comparison between seismic Earth structures and mantle flow models based on radial correlation functions, *Science, 261*, 1427-1431, 1993.

Kawakatsu, H., and F. Niu, Seismic evidence for a 920-km discontinuity in the mantle, *Nature, 371*, 301-305, 1994.

Kawakatsu, H., and F. Niu, Depth variation of the "920-km discontinuity" in the mid-mantle, *Ann. Geophys., 14*, 1-43, 1996.

Kellogg, L. H., B. H. Hager, and R. D. van der Hilst, Compositional stratification in the deep mantle, *Science, 283*, 1881-1884, 1999.

Lancaster, P., and K. Salkauskas, *Curve and Surface Fitting*, Academic, San Diego, Calif., 1990.

Li, X.-D., and B. Romanowicz, Comparison of global waveform inversions with and without considering cross-branch model coupling, *Geophys. J. Int., 121*, 695-709, 1995.

Li, X.-D., and B. Romanowicz, Global mantle shear velocity model developed using nonlinear asymptotic coupling theory, *J. Geophys. Res., 101*, 22,245-22,272, 1996.

Liu, X.-F., The three-dimensional shear-wave velocity structure of the Earth's lower mantle, thesis, 202 pp., Harvard Univ., Cambridge, Mass., 1997.

Liu, X.-F., and A.M. Dziewonski, Global analysis of shear wave velocity anomalies in the lowermost mantle, in *Core-Mantle Boundary, Geophys. Monogr. Ser.*, vol.28, edited by M. Gurnis, pp.21-36, AGU, Washington, D.C., 1998.

Machetel, P., and P. Weber, Intermittent layered convection in a model mantle with an endothermic phase change at 670 km, *Nature, 350*, 55-57, 1991.

Masters, G., T. H. Jordan, P. G. Silver, and F. Gilbert, Aspherical Earth structure from fundmental spheroidal-mode data, *Nature, 298*, 609-613, 1982.

Masters, G., H. Bolton, and P. Shearer, Large-scale 3-dimensional structure of the mantle, *Eos Trans. AGU, 72*(14), Spring Meet. Suppl., 201, 1992.

Masters, G., S. Johnson, G. Laske, and H. Bolton, A shear-

velocity model of the mantle, *Philos. Trans. R. Soc. London, 354*, 1385-1411, 1996.

Masters, G., G. Laske, A. Dziewonski, and L. Boschi, Towards a spherical reference Earth model, *Eos Trans. AGU, 80*(46), Fall Meet. Suppl. F27, 1999.

McNutt, M., The mantle's lava lamp, *Nature, 402*, 739-740, 1999.

Mégnin, C., and B. Romanowicz, The 3D shear velocity structure of the mantle from the inversion of body, surface, and higher mode waveforms, *Geophys. J. Int.*, in press, 2001.

Montagner, J.-P., Regional three-dimensional structures using long-period surface waves, *Ann. Geofis., 4*, 283-294, 1986.

Montagner, J.-P., and T. Tanimoto, Global anisotropy in the upper mantle inferred from the regionalization of phase velocities, *J. Geophys. Res., 95*, 4797-4819, 1990.

Montagner, J.-P., and T. Tanimoto, Global upper mantle tomography of seismic velocities and anisotropies, *J. Geophys. Res., 96*, 20,337-20,351, 1991.

Mooney, W., G. Laske, and G. Masters, A new global crustal model at 5 x 5 degrees: CRUST-5.1, *J. Geophys. Res., 103*, 727-747, 1998.

Peterson, N., J. Gossler, R. Kind, K. Stammler, and L. Vinnik, Precursors to *SS* and structure of the transition zone of the northwest Pacific, *Geophys. Res. Lett., 20*, 281-284, 1993.

Phipps Morgan, J., and P. M. Shearer, Seismic constraints on mantle flow and topography of the 660-km discontinuity, evidence for whole mantle convection, *Nature, 365*, 506-511, 1993.

Revenaugh, J., and T. H. Jordan, A study of mantle layering beneath the western Pacific, *J. Geophys. Res., 94*, 5787-5813, 1989.

Revenaugh, J., and T. H. Jordan, Mantle layering from *ScS* reverberation, 2, The transition zone, *J. Geophys. Res., 96*, 19,763-19,780, 1991.

Ricard, Y., M. Richards, C. Lithgow-Bertelloni and Y. Le Stunff, A geodynamic model of mantle density heterogeneity, *J. Geophys. Res., 98*, 21,895-21,909, 1993.

Ringwood, A. E., Role of the transition zone and 660 km discontinuity in mantle dynamic, *Phys. Earth Planet. Inter., 86*, 5-24, 1994.

Ritsema, J., H. J. Van Heijst, and J. H. Woodhouse, Complex shear wave velocity structure imaged beneath Africa and Iceland, *Science, 286*, 1925-1928, 1999.

Shearer, P. M., Global mapping of upper mantle reflectors from long-period *SS* precursors, *Geophys. J. Int., 115*, 878-904, 1993.

Shearer, P. M., and T. G. Masters, Global mapping of topography on the 660-km discontinuity, *Nature, 355*, 791-796, 1992.

Su, W.-J., and A. M. Dziewonski, Predominance of long-wavelength heterogeneity in the mantle, *Nature, 352*, 121-126, 1991.

Su, W.-J., and A. M. Dziewonski, Simultaneous inversion for 3-D variations in shear and bulk velocity in the mantle, *Phys. Earth Planet. Inter., 100*, 135-156, 1997.

Su, W.-J., R. L. Woodward, and A. M. Dziewonski, Degree-12 model of shear velocity heterogeneity in the mantle, *J. Geophys. Res., 99*, 6945-6980, 1994.

Tackley, P. J., Mantle convection and plate tectonics: toward an integrated physical and chemical theory, *Science, 288*, 2002-2007, 2000.

Tackley, P. J., D. J. Stevenson, G. Glatzmaier, and G. Schubert, Effects of an endothermic phase transition at 670-km in a spherical model of convection in the Earth's mantle, *Nature, 361*, 699-704, 1993.

Tackley, P. J., D. J. Stevenson, G. A. Glatzmaier, and G.

Schubert, Effects of multiple phase transitions in a 3-D spherical model of convection in the Earth's mantle, *J. Geophys. Res.*, *99*, 15,877-15,901, 1994.

Tanimoto, T., Long-wavelength *S*-wave velocity structure throughout the mantle, *Geophys. J. Int.*, *100*, 327-336, 1990.

Tarantola, A., and B. Valette, Generalized nonlinear inverse problems solved using the least squares criterion, *Rev. Geophys.*, *20*, 219-232, 1982.

Trefethen, L. N., and D. Bau, *Numerical Linear Algebra*, Soc. for Ind. and Appl. Math., Philadelphia, Penn., 1997.

van der Hilst, R., and H. Kárason, Compositional heterogeneity in the bottom 1000 kilometers of Earth's mantle: toward a hybrid convection model, *Science*, *283*, 1885-1888, 1999.

van der Hilst, R., R. Engdahl, W. Spakman, and G. Nolet, Tomographic imaging of subducted lithosphere below northwest Pacific island arcs, *Nature*, *353*, 37-43, 1991.

van der Hilst, R., S. Widiyantoro, and E. R. Engdahl, Evidence for deep mantle circulation from global tomography, *Nature*, *396*, 578-584, 1997.

van der Voo, R., W. Spakman, and H. Bijwaard, Mesozoic subducted slab under Siberia, *Nature*, *397*, 246-249, 1999.

Vidale, J. E., Geophysics; a mystery in the mantle, *Nature*, *372*, 288, 1994.

Vinnik, L. P., R. A. Avetisjan, and N. G. Mikhailova, Heterogeneities in the mantle transition zone from observations of *P*-to-*SV* converted waves, *Phys. Earth Planet. Inter.*, *33*, 149-163, 1983.

Wang, Z., and F. A. Dahlen, Spherical-spline parameterization of three-dimensional Earth models, *Geophys. Res. Lett.*, *22*, 3099-3102, 1995.

Woodhouse, J. H., and A. M. Dziewonski, Mapping the upper mantle: Three dimensional modeling of earth structure by inversion of seismic waveforms, *J. Geophys. Res.*, *89*, 5953-5986, 1984.

Woodhouse, J. H., and A. M. Dziewonski, Three dimensional mantle models based on mantle wave and long period body wave data, *Eos Trans. AGU*, *67*(16), 307, 1986.

Woodhouse, J. H., and A. M. Dziewonski, Seismic modeling of the Earth's large-scale three dimensional structure, *Philos. Trans. R. Soc. London*, *328*, 291-308, 1989.

Woodward, R. L., and G. Masters, Global upper mantle structure from long-period differential travel-times, *J. Geophys. Res.*, *96*, 6351-6377, 1991a.

Woodward, R. L., and G. Masters, Lower-mantle structure from *ScS − S* differential travel-times, *Nature*, *352*, 231-233, 1991b.

Woodward, R. L., A. M. Forte, W.-J. Su, and A. M. Dziewonski, Constraints on the large-scale structure of the Earth's mantle, in *Chemical Evolution of the Earth and Planets*, *Geophys. Monogr. Ser.*, vol.74, edited by E. Takahashi, R. Jeanloz, and D. Rubie, pp.89-109, AGU, Washington, D.C., 1993.

Woodward, R. L., A. M. Dziewonski, and W. R. Peltier, Comparisons of seismic heterogeneity models and convective flow calculations, *Geophys. Res. Lett.*, *21*, 325-328, 1994.

Wysession, M. E., E. A. Okal and C. R. Bina, The structure of the core-mantle boundary from diffracted waves, *J. Geophys. Res.*, *97*, 8749-8764, 1992.

Zhang, Y.-S., and T. Tanimoto, High-resolution global upper mantle structure and plate tectonics, *J. Geophys. Res.*, *98*, 9793-9823, 1993.

Zhou, H.-W, and R. W. Clayton, *P* and *S* wave travel time inversions for subducting slab under the island arcs of the northwest Pacific, *J. Geophys. Res.*, *95*, 6829-6851, 1990.

A. M. Dziewonski, G. Ekström, Y. J. Gu, and W.-J. Su, Department of Earth and Planetary Sciences, Harvard University, Cambridge, MA 02138. (dziewons@eps.harvard.edu; ekstrom@eps.harvard.edu; gu@eps.harvard.edu; su@eps.harvard.edu)